1 # Retrieval Algorithm for Aerosol Effective Height from the

2 # Geostationary Environment Monitoring Spectrometer (GEMS)

3

4 Sang Seo Park[1,*], Jhoon Kim[2], Yeseul Cho[2], Hanlim Lee[3], Junsung Park[3], Dong-Won

5 Lee[4], Won-Jin Lee[4], Deok-Rae Kim[4]

6 [1] Department of Urban and Environmental Engineering, Ulsan National Institute of Science

7 and Technology, Ulsan, Korea

8 [2]Department of Atmospheric Sciences, Yonsei University, Seoul, Korea

9 [3]Division of Earth and Environmental System Sciences, Pukyong National University, Busan,

10 South Korea

11 [4]Envionment Satellite Center, National Institute of Environmental Research, Incheon, Korea

12

13

14

15 [*]Corresponding author. Sang Seo Park (sangseopark@unist.ac.kr)

16

17

20

21

Abstract

An algorithm for aerosol effective height (AEH) was developed for operational use with observations from the Geostationary Environment Monitoring Spectrometer (GEMS). The retrieval technique uses the slant column density of the oxygen dimer (O_2-O_2) at 477 nm, which is converted into AEH after retrieval of aerosol and surface optical properties from GEMS operational algorithms. The AEH retrieval results show significant AEH values and continuously monitor aerosol vertical height information in severe dust plumes over East Asia, and the collection of plume height information for anthropogenic aerosol pollutants over India. Compared to the AEH retrieved from Cloud-Aerosol Lidar with Orthogonal Polarization (CALIOP), the retrieval results show bias of -0.03 km with a standard deviation of 1.4 km for the AEH difference over the GEMS observation domain from January to June, 2021. The AEH difference depends on aerosol optical properties and surface albedo. Compared to the aerosol layer height obtained from the tropospheric monitoring instrument (TROPOMI), differences of 1.50 ± 1.08 km, 1.59 ± 1.22 km, and 1.71 ± 1.24 km were obtained for pixels with single scattering albedo (SSA) < 0.90, 0.90 < SSA < 0.95, and SSA > 0.95, respectively.

Keywords: aerosol effective height, aerosol optical depth, environmental satellite, GEMS

1. Introduction

Since the launch of the Total Ozone Mapping Spectrometer (TOMS) on Nimbus-7, ultraviolet (UV)-visible satellite measurements have been used for environmental monitoring of the distribution and reaction processes of pollutants (e.g., anthropogenic aerosols, tropospheric ozone, NO_2, and SO_2). Measurements from environmental satellites have been used to estimate gaseous species in the atmosphere, resulting in vertical column integrated amounts. However, these column-integrated amounts and associated surface concentrations have uncertainty due to simultaneous changes in optical path length associated with the vertical distribution of target species and amounts of scattering materials (clouds and aerosols) present. In addition, aerosol vertical information is also important information for the application for tropospheric concentration of aerosols. For example, aerosol height information in the free troposphere is particularly important for aviation safety by affecting the visibility. Also, scientific applications including radiative forcing studies, long-range transport modelling and studies of cloud formation processes have been used aerosol vertical information as an input parameter.

Environmental satellite sensors, that measure UV-visible wavelength, have been used the UV aerosol index (UVAI) for aerosol detection (e.g., Buchard *et al.*, 2015; Herman *et al.*, 1997; Torres *et al.*, 1998, 2002; Prospero *et al.*, 2000; de Graaf *et al.*, 2005). Furthermore, scattering radiative index values were investigated for the possibility of the cloud signal detection (Penning de Vries *et al.*, 2009, 2015; Kooreman *et al.*, 2020; Kim *et al.*, 2018). However, these indices only have qualitative characteristics and limitations to identify aerosol amounts.

For the quantitative estimation, measurements of aerosol optical depth (AOD) and

67　radiative cloud fraction have also been retrieved from pixel-based radiance data in UV-

68　visible wavelength range. Recently, various aerosol retrieval algorithms have been

69　developed to be applied in passive satellite sensors. These algorithms focus on

70　improved trace gas retrieval as well as direct monitoring of aerosol properties, such as

71　AOD and single scattering albedo (SSA) (e.g., Ahn *et al.*, 2014; Kim *et al.*, 2020; Torres

72　et al., 2020).

73　　Although the algorithms developed for environmental satellite sensors indicate the

74　presence and amount of scattering materials, the accuracy of these retrieval algorithms

75　for trace gases is affected by the relative vertical distributions between trace gases and

76　scattering materials (e.g., Lorente *et al.*, 2017; Hong *et al.*, 2017). For this reason,

77　estimating cloud vertical parameters is important. For cloud vertical information, cloud

78　height information has been estimated simultaneously with cloud optical depth and

79　radiative cloud fraction data using the rotational Raman scattering (Joiner and Vasilkov,

80　2006; Vasilkov *et al.*, 2008; Joiner and Bhartia, 1995) and absorption intensity of the

81　oxygen dimer (O_2-O_2) (Accarreta *et al.*, 2004; Vasilkov *et al.*, 2018; Choi *et al.*, 2021)

82　combined with normalized radiance.

83　　Similarly, the aerosol vertical distribution can be estimated using the oxygen

84　absorption bands, such as the O_2-O_2 (Park *et al.*, 2016; Chimot *et al.*, 2017; Choi *et al.*,

85　2019, 2020), O_2-A (Dubisson *et al.*, 2009; Geddes and Boesch, 2015; Sanders *et al.*,

86　2015; Zeng *et al.*, 2020), and O_2-B (Ding *et al.*, 2016) bands, as well as combinations of

87　these bands (Sanghavi *et al.*, 2012; Chen et al., 2021). In addition, an algorithm for

88　aerosol vertical information has been developed based on hyperspectral UV-visible

89　radiance from satellite observation. Nanda *et al.* (2018) demonstrated the possibility of

90　aerosol height retrieval from the O_2-A band developed an algorithm using Tropospheric

91 Monitoring Instrument (TROPOMI) (Sanders and de Haan, 2016; Nanda *et al.*, 2020)

92 and implemented the algorithm operationally.

93 However, the vertical distribution of aerosol is difficult to assess because of its large

94 spatio-temporal variability. Although the Cloud-Aerosol Lidar with Orthogonal

95 Polarization (CALIOP) provided the aerosol vertical distribution with high vertical

96 resolution (Omar et al., 2009), other passive satellite sensors are only able to estimate

97 the representative parameter of aerosol height. Veihelmann et al. (2007) showed that the

98 number of degrees of freedom of signal for aerosol is 2~4 for most of satellite

99 observation conditions by the ozone monitoring instrument (OMI). In addition, the

100 number of degrees of freedom is not exceeded to 3 from the shortwave satellite

101 measurements (e.g., Rao et al., 2019; Choi et al., 2021). It means that the amount of

102 information for aerosol vertical distribution has a limitation for satellite sensor. Because

103 of limitation for describing the aerosol vertical information, aerosol layer height (ALH)

104 (Nanda et al., 2018) or aerosol effective height (AEH) (Park et al., 2016) were defined

105 to retrieve the aerosol vertical information from the passive satellite sensors.

106 The Geostationary Environment Monitoring Spectrometer (GEMS), which was

107 launched by South Korea in February 2020, retrieves data related to major trace gases

108 and aerosol properties (Kim *et al.*, 2020). The main purpose of GEMS is to monitor air

109 quality, and aerosol properties are targets of such monitoring over East Asia. For this

110 reason, the GEMS aerosol algorithm was developed as multiple operational products.

111 Aerosol properties are obtained for the purposes of monitoring surface air quality and

112 aerosol effects for the air mass factor (AMF) calculation. In addition to the aerosol

113 optical property algorithm, the GEMS aerosol product is applied to the aerosol vertical

114 information, AEH. For the possibility for development of an AEH retrieval algorithm,

5

115   Park *et al.* (2016) conducted theoretical sensitivity testing of AEH retrieval using solely

116   the O_2-O_2 absorption band along with aerosol and surface properties. Overall, the

117   sensitivity of AEH retrieval was strongly affected by SSA, AOD, and aerosol types

118   including optical and size properties, and the error budget for AEH retrieval using the

119   O_2-O_2 band was 739 ~ 1276 m. In addition, case studies of AEH during dust transport

120   over East Asia were conducted using radiance data from the Ozone Monitoring

121   Instrument (OMI) and aerosol optical properties from the Moderate Resolution Imaging

122   Spectroradiometer (MODIS).

123   Based on theoretical considerations and case results of previous studies, we introduce

124   an operational retrieval algorithm for AEH. Section 2 introduces the details of satellite

125   sensors for the comparison and colocation method in this study. Section 3 describes the

126   details of the AEH retrieval algorithm for GEMS and provides a list of the detailed input

127   parameters. Section 4 reports retrieval results based on case studies of aerosol transport,

128   and section 5 contains long-term validation results based on CALIOP and TROPOMI

129   data. Finally, in section 6, the summary and main conclusions are presented.

130

131 **2. Data**

132 **2.1 GEMS**

133   The GEMS is onboarding the Geostationary Korea multipurpose satellite 2B (GK2B)

134   as orbiting at 128.2°E, and scans from 145°E to 75°E with north-south coverage of

135   5°S~45°N. The GK2B observation schedule shares the GEMS and the Geostationary

136   Ocean Color Imager 2 (GOCI2), and the GEMS scan the 30 minutes duration from

137   every hour from 45 minutes to 15 minutes during daytime. The standard spatial

138   resolution of GEMS is 7 km × 8 km. The spectral resolution and sampling are

139 respectively 0.6 nm with full-width and half-maximum (FWHM) and 0.2 nm with

140 spectral range of 300~500 nm.

141   The GEMS Level 2 aerosol operational algorithm (L2AERAOD) retrieves the aerosol

142 index (AI) values for UV and visible wavelengths, as well as AOD and SSA with

143 considering the aerosol types (National Institute of Environmental Research, 2020a).

144 The aerosol types are defined as absorbing, non-absorbing, and dust types by using the

145 classification methods based on the UV and visible AIs (e.g., Go et al., 2020). Park *et al.*

146 (2016) noted that the error budget of AEH is significantly affected by uncertainty in

147 AOD and SSA and by the misclassification of aerosol types, which is directly related to

148 the optical property and size information. Overall, the error for AEH is ranged from

149 739~1276 m under the AOD error of 0.2, particle size error of 20%, SSA error of 10%,

150 and surface albedo error of 0.02 (Park et al., 2016). The main variables causing errors

151 for AEH retrieval can be obtained from the L2AERAOD results. Therefore, the

152 L2AERAOD results for AOD at 550 nm and SSA at 443 nm were adopted as input data

153 for aerosol properties.

154   Although L2AERAOD retrieved their own surface reflectance for accurate separation

155 of surface signals from total reflectance at the top of the atmosphere (TOA), the

156 standard product for surface reflectance (L2SFC) (National Institute of Environmental

157 Research, 2020b) was also independently retrieved from GEMS radiance/irradiance data

158 with specific temporal periods. L2SFC is the reference product for spectral surface

159 reflectance. The L2SFC retrieves the surface reflectivity in multiple spectral channels

160 and provides the black surface reflectivity (BSR) and bi-directional reflectance

161 distribution function (BRDF) based on the original pixel resolution. Recently, L2SFC

162 accurately estimated surface reflectance in near real time in operation. For this reason,

7

163   L2SFC was used as reference data for the surface products for the air mass factor

164   estimation to all trace gas retrieval algorithms. Similarly, the AEH retrieval algorithm

165   also uses L2SFC as a reference surface reflectance in operation. Specifically, the BSR

166   value at 477 nm is used as the surface reflectance input for AEH retrieval. However, this

167   study used the minimum reflectance under the Lambertian assumption to retrieve AOD

168   and AEH to coincide with the use of surface information on L2AERAOD and AEH

169   retrieval.

170

171   **2.2. TROPOMI**

172   TROPOMI is a nadir-viewing spectrometer, the only payload of the Sentinel-5

173   Precursor (S5P), measuring radiance in the UV, visible, near-infrared, and the shortwave

174   IR (Veefkind et al., 2012). The S5P crosses the equator at 13:30 local time in a polar

175   orbit with ascending node providing near-global daily coverage. The aerosol layer

176   height product from TROPOMI (AER_LH) retrieves vertically localized aerosol layers

177   in free troposphere with cloud free condition by using the level 1b earth radiance

178   measurements from 758 to 770 nm (de Graaf *et al.*, 2022). The definition of ALH from

179   TROPOMI is the optical centroid layer height of the plume above sea level. Spectral fit

180   estimation of reflectance around the O_2-A band is based on a neural network for the

181   forward model calculation for simulated condition. After cloud masking to avoid the

182   cloud affected pixels, an optimal estimation method was used to retrieve the aerosol

183   layer height parameters for the inversion method from observation. During the radiance

184   fitting, the ALH and AOD are fitted parameters, but other aerosol parameters, such as

185   SSA, layer thickness, and scattering phase function, are assumed to be fixed values

186   (Nanda et al., 2020). Furthermore, the ALH retrieval has limitation to the aerosol plume

187   with higher than 12 km, because the ALH neural network method is currently adopted

188   to the plume pressure range of 75~1000 hPa (Michailidis et al., 2023).

189   Main purpose of the AER_LH product is the retrieval of aerosol layers in the free

190   troposphere (desert dust, biomass burning, and volcanic ash) (Michailidis et al., 2023).

191   The target requirement on the accuracy and precision is 0.5 km or 50 hPa, and the

192   threshold requirement is 1 km or 100 hPa under the elevated aerosol plumes with cloud-

193   free conditions (de Graaf et al., 2022, Veefkind et al., 2012). However, the TROPOMI

194   ALH product has strong dependence of the surface albedo, especial to the bright

195   surfaces (Sanders et al., 2015). From Michailidis et al. (2023), a mean bias of -

196   0.51±0.77 and -2.27±1.17 km is estimated over ocean and land, respectively. In this

197   study, we use version 02.04.00 of the TROPOMI offline level 2 AER_LH product

198   (European Space Agency, 2021) with the spatial resolution is 3.5 km × 5.5 km at nadir

199   viewing geometry.

200

201   **2.3. CALIOP**

202   The CALIOP is a spaceborne lidar onboard the Cloud-Aerosol Lidar and Infrared

203   Pathfinder Satellite Observations (CALIPSO) to measure the vertical information of

204   aerosol and cloud with estimating the optical properties. The CALIOP has two different

205   wavelength channels (532 and 1064 nm) by using the Nd:YAG laser to generate the

206   signals (Winker et al., 2009). The orbit for CALIPSO is Sun synchronous orbit

207   constelled to the A-train with period of 98.3 minutes by ascending node. It crosses the

208   equator at 13:30 local time. To cover the GEMS observation area, we used CALIOP

209   data of 3~4 orbits per day. For the vertical information, the resolution for vertical

210   sampling is 30 m below 8 km altitude, and 60 m from 8 to 20 km altitude, respectively.

211 Although the CALIOP retrieves the data with extremely high horizontal and vertical

212 resolutions, the spatial coverage is narrow because the footprint of the CALIOP is about

213 90m at the Earth surface. In this study, the data of Level 2 aerosol profile product (APro,

214 version 3.41) was used (Tackett et al., 2018. The aerosol profile product simultaneously

215 includes both aerosol and cloud optical depth. In addition, extinction quality flag

216 (Extinction_QC_Flag) data shows the quality of extinction profile. In this study, we

217 checked and used to the quality flag value at 532 nm for the aerosol extinction

218 coefficient profile data. The AOD from CALIOP is vertically integrated aerosol

219 extinction coefficient from surface to top of atmosphere, and representative layer height

220 parameters (ALH and AEH) are directly estimated by using the vertical profile of

221 aerosol extinction coefficient at 532 nm to minimize the spectral discrepancy of aerosol

222 extinction. For the ALH retrieval, we adopted mean extinction height from the CLIOP

223 extinction coefficient profile (e.g., Koffi et al., 2012; Xu et al., 2019). Furthermore, the

224 AEH adopted the same method as CALIOP for estimating the ALH, with only changes

225 in the height definition.

226

227 **2.4 Data Selection and Colocation**

228 In this study, we used the data within 75°E~145°E for east-west and 5°S~45°N for

229 north-south direction, which is observation area of GEMS. For spatial colocation, we

230 selected pixels for which distance between GEMS and CALIOP (or TROPOMI)

231 observations was less than 50 km. From Park et al. (2020), the spatial scales for AOD

232 validation are 30~40 km. To ensure that the number of retrieved observation pixels, we

233 relax the spatial limits for collocation matching. In addition, only the closest 10% of

234 pixels were used. Given the different orbital characteristics of CALIOP (or TROPOMI)

and GEMS, temporal colocation was also considered. During the period of image scanning from east to west over Asia by GEMS, CALIOP and TROPOMI pass through the GEMS observation area from south to north every 98.3 minutes. On average, two low earth orbit (LEO) satellites pass three to four orbits through the GEMS scan area during a single day of daytime observation. To consider these different orbital characteristics, only observations taken within ±1 hour of the GEMS observation time was selected for temporal colocation. As GEMS observes hourly, collocated pixels between the two satellites shift from east to west over time.

To ensure the accuracy of ALH from TROPOMI, only pixels with quality assurance (QA) values of 1.0 were used. To minimize the cloud contamination, the TROPOMI ALH product uses the VIIRS cloud mask information and cloud parameters from the Fast Retrieval Scheme for Clouds from the Oxygen A-band (FRESCO). To consider the cloud contamination for the aerosol products, in addition, the VIIRS cirrus cloud reflectance (viirs_cirrus_reflectance < 0.4), VIIRS cloud mask (viirs_cloud_mask < 0.1), and cloud fraction from the FRESCO (cloud_fraction < 0.1) are considered in this study (Michailidis et al., 2023). However, de Graaf *et al.* (2022) showed that respective cloud masking method have difficulty detecting various clouds. For this reason, accuracy problem of ALH by the cloud contamination is still remained. From the previous studies, the UVAI is used as the threshold to define the absorbing aerosol pixels (e.g., Chen et al., 2021; Griffin et al., 2020; Michailidis et al., 2023; Sanders et al., 2015). However, the GEMS aerosol product is retrieved not only the absorbing aerosols, but also the non-absorbing aerosols. For this reason, the UVAI is not used to the threshold of aerosol pixel identification. Instead, we adopted the larger than 0.3 for AOD at 443 nm from GEMS to identify both absorbing and non-absorbing aerosol loading.

259

3. AEH retrieval algorithm

AEH is a layer height parameter that considers the penetration of photons into the aerosol layer. In this study, the AEH product from GEMS is defined as the height with aerosol extinction integrated from the surface of $(1\text{-}e^{-1}) \times$ AOD, and a detailed definition of AEH was introduced by Park *et al.* (2016). Numerous previous studies have used the aerosol top layer height (Kohkanovsky and Rozanov, 2010) or middle layer height (i.e. ALH or centroid height) (e.g., Sanders *et al.*, 2015; Nanda *et al.*, 2020) as the aerosol vertical layer parameter. AEH is similar to the aerosol top layer height but with a slight bias.

For AEH retrieval, the vertical distribution assumption is also important. The Gaussian Density Fitting (GDF) distribution, which is a modified Gaussian distribution structure, is assumed for AEH retrieval. The full-width at half-maximum (FWHM) of the aerosol layer is 1 km. Schematic description of AEH and other aerosol vertical parameters are shown in Figure 1. Based on the assumptions about the aerosol vertical distribution, the AEH value is higher than the peak height of the Gaussian distribution and lower than the aerosol top layer height. Otherwise, aerosol layer height (ALH) in this study is defined as the height integrated aerosol extinction from the surface reaching half of AOD (i.e., $0.5 \times$ AOD). Therefore, the ALH is same to the peak height for the vertical profile condition as shown in Figure 1.
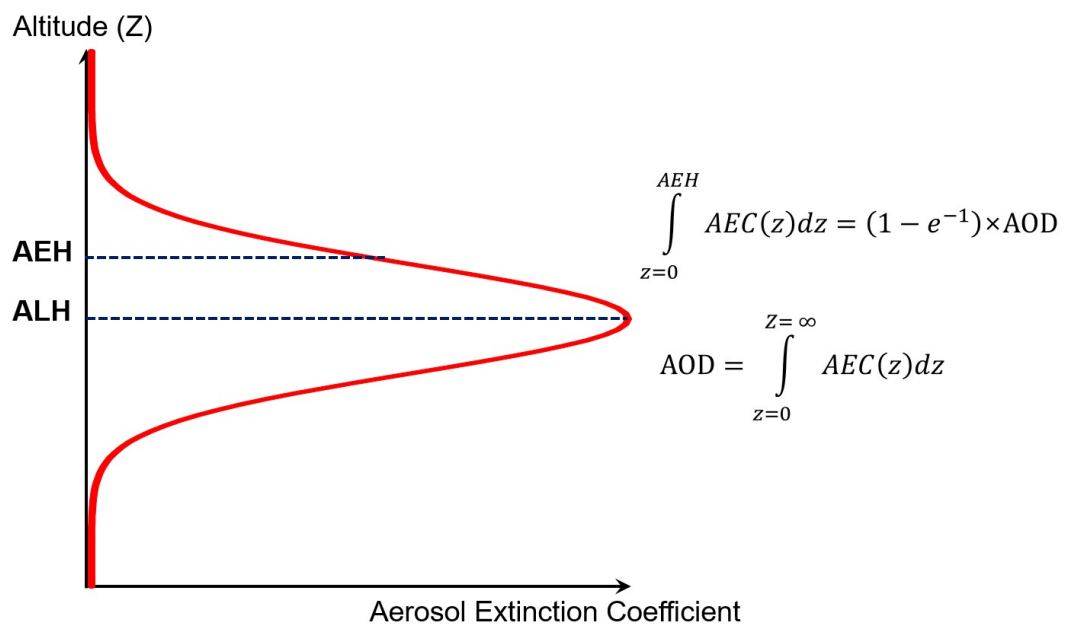
12

Figure 1. A schematic illustration of AEH and ALH definitions in an idealized Gaussian shape of aerosol vertical distribution.

$$\int_{z=0}^{AEH} AEC(z)dz = (1 - e^{-1}) \times AOD$$

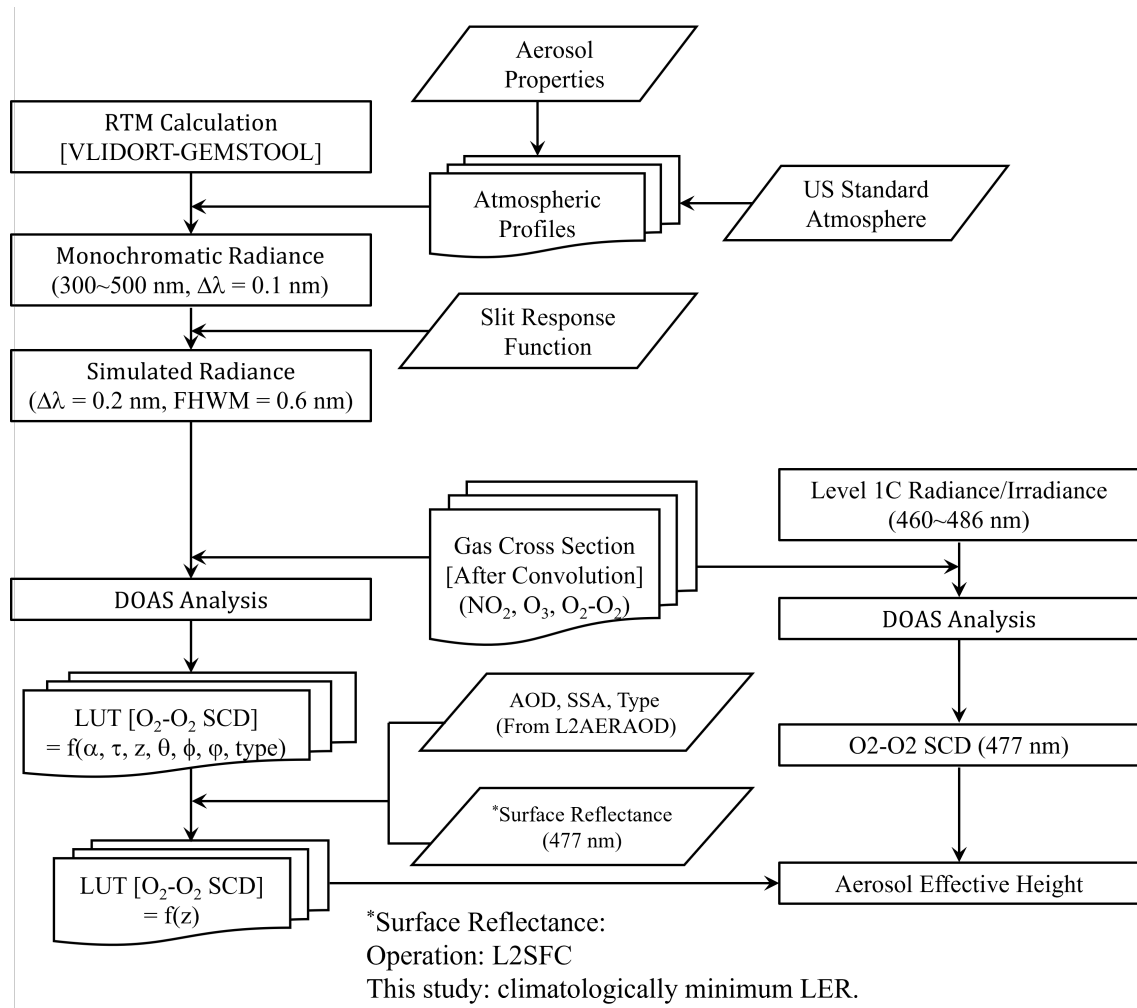$$AOD = \int_{z=0}^{Z=\infty} AEC(z)dz$$

Figure 2. Flowchart of the AEH retrieval algorithm for GEMS satellite observation.

Figure 2 shows the overall flowchart of the AEH algorithm for GEMS satellite. The AEH algorithm for GEMS composed a look-up table (LUT) development between AEH and O_2-O_2 SCD by the radiance simulation and SCD estimation from the satellite radiance. The LUT is a function of observation geometries [solar zenith angle (SZA; θ), viewing zenith angle (VZA; Φ), relative azimuth angle (RAA; φ)], surface altitude (z), surface albedo (α), AOD (τ), and aerosol type. During the radiance simulation, the radiance is monochromatically simulated and simulated monochromatic radiance is

14

convolved as considering the spectral response of GEMS instruments. For AEH estimation, the radiance information is finally converted to the AEH values by using the differential optical absorption spectroscopy (DOAS) method. DOAS method is identification technique for the spectral absorption signals from radiance information and detailed principle and information is explained by Platt (1994). DOAS method has been frequently used to estimate the amount of trace gases (i.e., SCD of trace gas) from ground (e.g., Cheng et al., 2023; Irie et al., 2008; Platt and Stutz, 2008; Wagner et al., 2011; Wang et al., 2017) and satellite (e.g., Kwon et al., 2019; Li et al., 2023; Wagner et al., 2007, 2010) measurements.

For AEH retrieval, the basic method is the identification of changes in optical path length caused by effective aerosol layer height variation. To measure the optical path length change, O_2-O_2 slant column density (SCD) retrieved by the DOAS method was used because the spectral coverage is limited to 300-500 nm (Park et al., 2016, Kim et al., 2020). In the GEMS product, the O_2-O_2 SCD at 477 nm absorption band is most useful absorption band because this absorption band is strongest absorption band within the GEMS spectral observation range. Detailed DOAS fitting parameter and setting information is provided in Table 1 for the estimation of O_2-O_2 SCD from both the simulation and observation data. For the O_2-O_2 SCD estimation at 477 nm, the fitting window is ranged from 460 to 486 nm to cover the full absorption structure of O_2-O_2. Within the fitting window, the absorptions of NO_2 and O_3 is significant. To describe these two absorbing species, temperature dependent cross section information are adopted. The temperature dependent cross section setting considers the stratosphere and troposphere, simultaneously.

316   **Table 1.** Details of fitting parameter for O_2-O_2 SCD estimation via the DOAS method.

Parameter	
Fitting window	460 – 486 nm
Absorption cross section	NO_2 at 220 and 294 K (Vandaele *et al.*, 1998)
	O_3 at 223, 243 and 293K (Bogumil *et al.*, 2001)
	O_2-O_2 at 293 K (Thalman and Volkamer, 2013)
	Ring

317   **Table 2.** Ratio between SCD error and the SCD of O_2-O_2 according to the polynomial

318   order and offset settings used for DOAS fitting.

Polynomial	Offset = none	Offset = 0th
2nd order	6.06 ± 2.07	6.79 ± 2.31
3rd order	6.32 ± 2.20	6.79 ± 2.32
4th order	7.86 ± 2.78	7.34 ± 2.85

319   To minimize the noise effect and improve DOAS fitting quality, the optimal settings

320   for fitting were also analyzed. Table 2 shows ratios of O_2-O_2 SCD error to the O_2-O_2

321   SCD for various polynomial and bias orders from observed radiance. The polynomial

322   and offset are basic fitting parameters for the DOAS fitting. Two parameters describe

323   the broadband spectral feature of radiance before identifying the gas absorption

324   structure. The ratio between SCD error and the SCD of O_2-O_2 is important to determine

325   the AEH retrieval quality. When the fitting error increase, the uncertainty of AEH is also

326   enhanced during the retrieval. For this reason, the setting with 2nd order of polynomial

327   and none offset was used for the O_2-O_2 SCD estimation from the GEMS radiance due to

328   the smallest fitting error.

329   In AEH estimation, other aerosol characteristics, including aerosol load and optical

330   properties, affect retrieval accuracy. From Park et al. (2016), uncertainty of AEH

331   retrieval result is largest by the SSA uncertainty. In addition, the AEH retrieval

332   uncertainty by the aerosol optical properties (e.g., AOD and phase function) and surface

333   albedo has dependence of observation geometries. After the estimation of O_2-O_2 SCD,

334   for this reason, conversion from O_2-O_2 SCD to AEH is an essential process. Table 3

335   shows the dimension of the LUT for the AEH retrieval algorithm. To calculate the LUT,

336   a linearized pseudo-spherical vector discrete ordinate radiative transfer model

337   (VLIDORT) version 2.6 was used (Spurr, 2013). During the radiative transfer model

338   simulation, reference wavelength for the SSA and AOD is assumed to be 440 nm. The

339   aerosol type is considered by the radiative absorptivity and size information, which is

340   based on the method from Lee et al. (2010). Based on the Lee et al. (2010), the aerosol

341   type is classified to absorbing, dust, and non-absorbing aerosol. Absorbing and non-

342   absorbing aerosol types are assumed to the fine-mode dominant particles. For the

343   spectral conversion of AOD, the angstrom exponent of 1.186, 0.222, and 1.179 are used

344   for absorbing, dust, and non-absorbing aerosol, respectively. Otherwise, the SSA is

345   assumed as the fixed value within the spectral range for O_2-O_2 estimation. Although the

346   center of O_2-O_2 absorption is 477 nm, the spectral discrepancy between model assumed

347   wavelength and center wavelength of O_2-O_2 absorption is assumed to be ignored in this

348   study. After calculating spectral radiance with 0.1 nm sampling, we performed the slit

349   response function of GEMS and sampling specification prior to the DOAS fitting. For

350   O_2-O_2 absorption, the absorption cross section used for the radiative transfer model

351   calculation is considered the temperature dependent absorption cross section (e.g., Park

352   *et al.*, 2017).

353   **Table 3.** The dimension of the LUT for the GEMS AEH retrieval algorithm used to

354   estimate AEH from O_2-O_2 SCD. (SZA: solar zenith angle, VZA: viewing zenith angle,

355   RAA: relative azimuth angle, SUR: surface reflectance).

Variable [unit]	No. of entries	Entries		
Spectral range [nm]	-	455~491 nm (0.1 nm interval)		
SZA [º]	7	0.01, 10, 20, 30, 40, 50, 60		
VZA [o]	7	0.01, 10, 20, 30, 40, 50, 60		
RAA [o]	10	0.01,20, 40, 60, 80, 100, 120, 140, 160, 180		
SUR	3	0.0, 0.05, 0.2		
AOD at 440 nm	11	0.04, 0.2, 0.4, 0.7, 1.0, 1.3, 1.6, 2.0, 2.5, 3.0, 5.0		
Refractive Index (Imaginary) at 440 nm	3×3	**Absorbing** (Real: 1.45)	0.000, 0.0074, 0.0314	
		Dust (Real: 1.53)	0.0, 0.0030, 0.0080	
		Non-Absorbing (Real: 1.41)	0.0, 0.0040, 0.0156	
AEH [km]	13	0.0 (Extrapolate), 0.2, 0.5, 1.0, 1.3,1.6, 2.0, 2.3, 2.7, 3.0, 3.5, 5.0, 10.0 (Extrapolate)		
Terrain Height [km]	2	0.0, 2.0		

(a)

Absorbing Type (Albedo = 0.05, SZA = 40, VZA=40, RAA=100)

(b)

Dust Type (Albedo = 0.05, SZA= 40, VZA=40, RAA=100)

(c)

Non-Absorbing Type (Albedo = 0.05, SZA= 40, VZA=40, RAA=100)
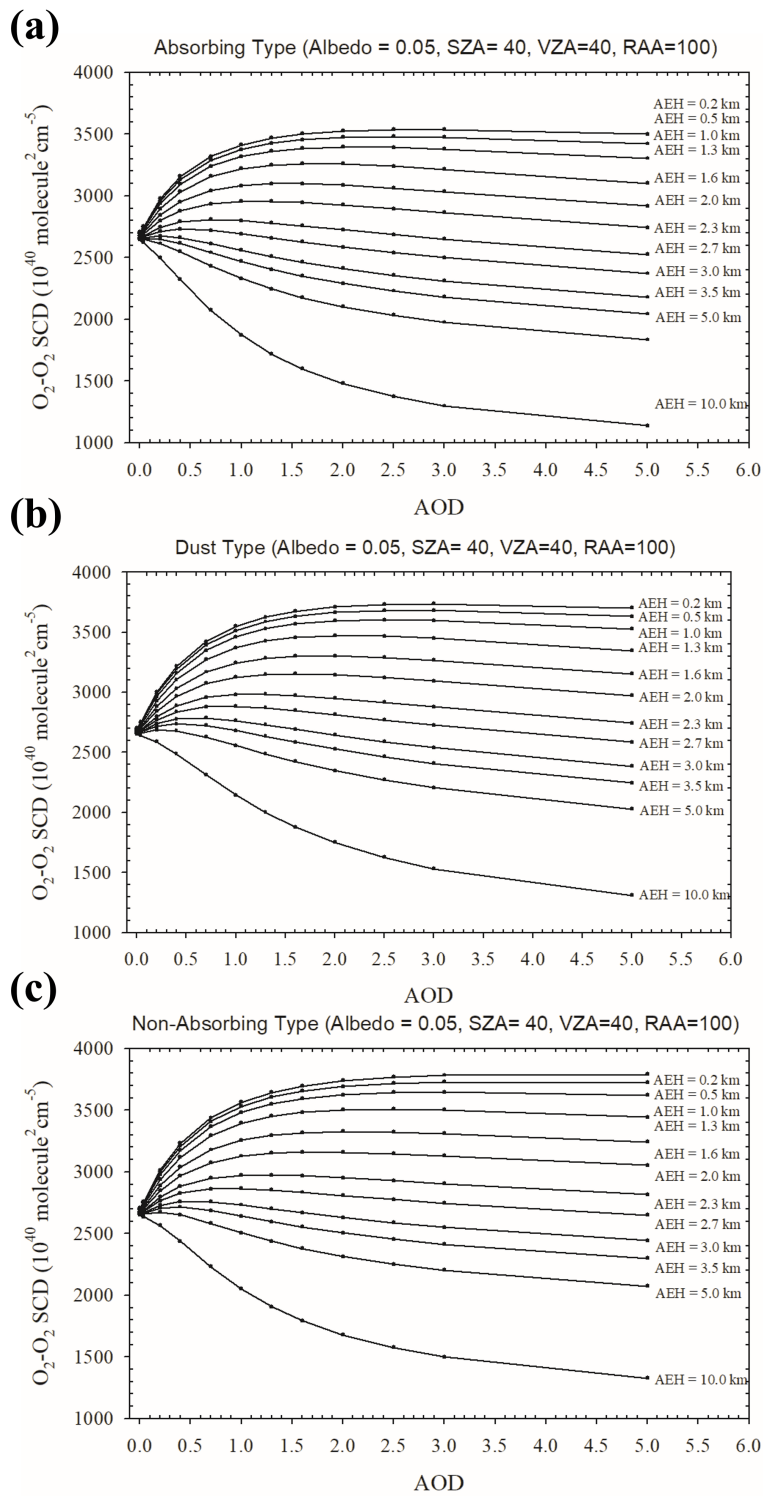
356

357 **Figure 3.** Example of LUT to retrieve the AEH according to (a) Absorbing, (b) Dust,

358 and (c) Non-Absorbing aerosol types.

359

360   Figure 3 shows the example of LUT to retrieve the AEH from O_2-O_2 SCD according

361   to the respective aerosol types and AOD. O_2-O_2 SCD decreases with increasing AEH for

362   all aerosol types and AOD (Park *et al.*, 2016). Similar to the previous study, the O_2-O_2

363   SCD sensitivity is enhanced at high AOD and absorbing aerosol cases from GEMS LUT.

364   In addition, the contrast of O_2-O_2 SCD is greater for absorbing aerosols than non-

365   absorbing aerosols. During the radiance passing through the aerosol layer, the absorbing

366   aerosol is more efficiently absorbed the radiance. For this reason, the effective optical

367   path length is significantly shorter for absorbing aerosols.

368   Although the surface reflectance and AOD are retrieved by the GEMS operational

369   products, retrieved values are always included the uncertainties. To consider the

370   retrieval error, the retrieval uncertainty of AEH was evaluated as the relative ratio of

371   SCD changes with respect to input variables. This ratio is defined by the relationship

372   between changes in SCD per unit AEH and changes in SCD due to uncertainties in input

373   variables. Figure 4 shows the AEH retrieval uncertainty based on the O_2-O_2 SCD LUT

374   with an AOD error of 0.2. The AOD error of 0.2 is twice the target accuracy of the

375   GEMS standard algorithm product. Because the O_2-O_2 SCD change is small in high

376   AOD, the AEH retrieval uncertainty is relatively small in high AOD condition. In

377   addition, the SCD sensitivity in high AEH is weak due to the vertical distribution

378   characteristics of O_2-O_2. Thus, the AEH uncertainty is up to 0.9 km at high AEH case in

379   moderate AOD cases (around 0.5~1.0).

380   Figure 5 shows the AEH retrieval uncertainty with the surface reflectance error of

381   0.02. Because surface reflection and aerosol scattering simultaneously affect the

382   increase in optical path length, surface reflectance uncertainty have a significant impact

383   especial to low AOD. The AEH retrieval error due to uncertainty in surface reflectance

384   is larger than 1 km in AOD < 0.4. In addition, the AEH error by the surface reflectance

385   uncertainty linearly decreases with increasing AOD, indicating relatively small impact

386   with aerosol height change.
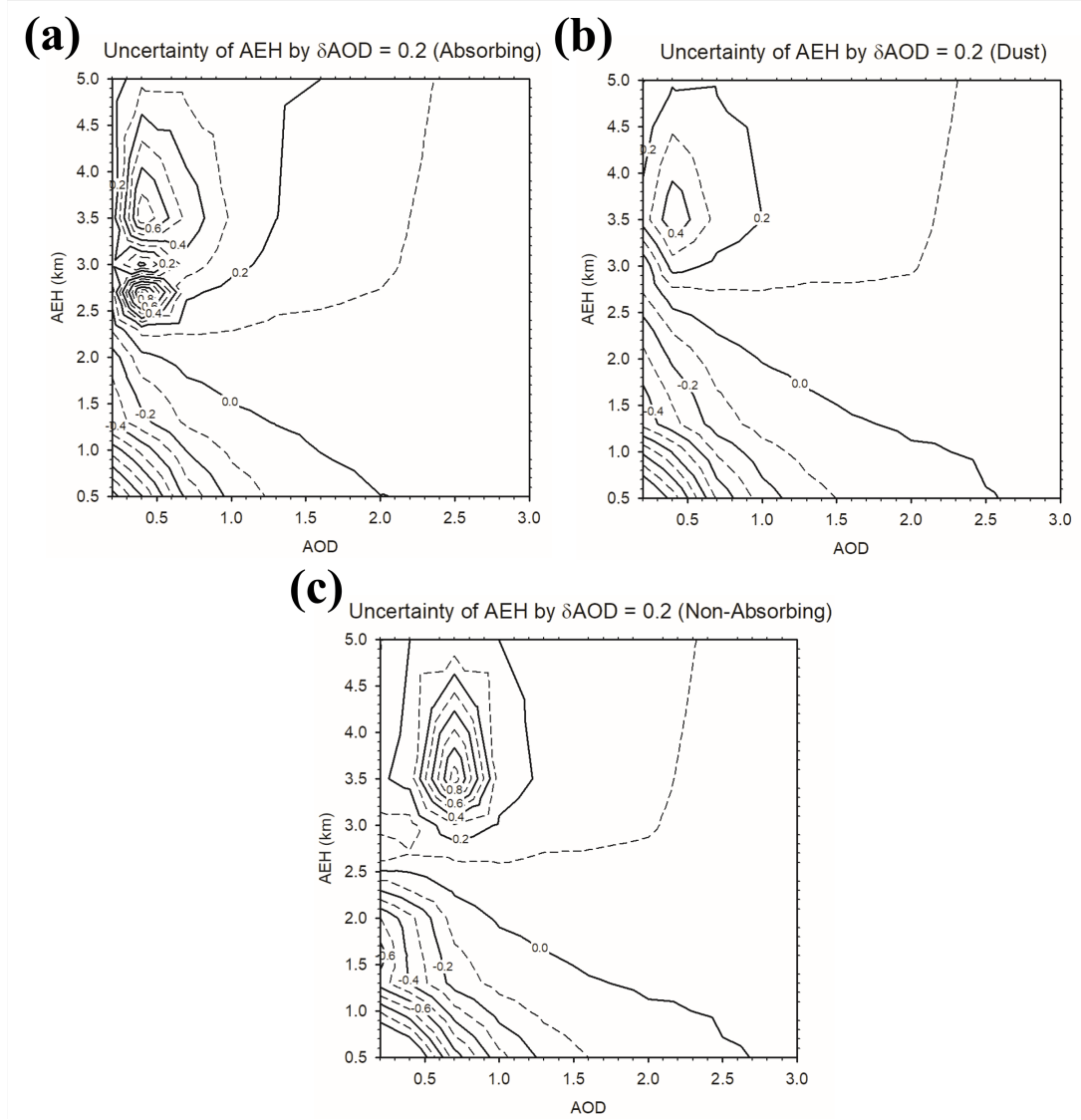
388   **Figure 4.** AEH retrieval uncertainty by the AOD error of 0.2 according to (a)

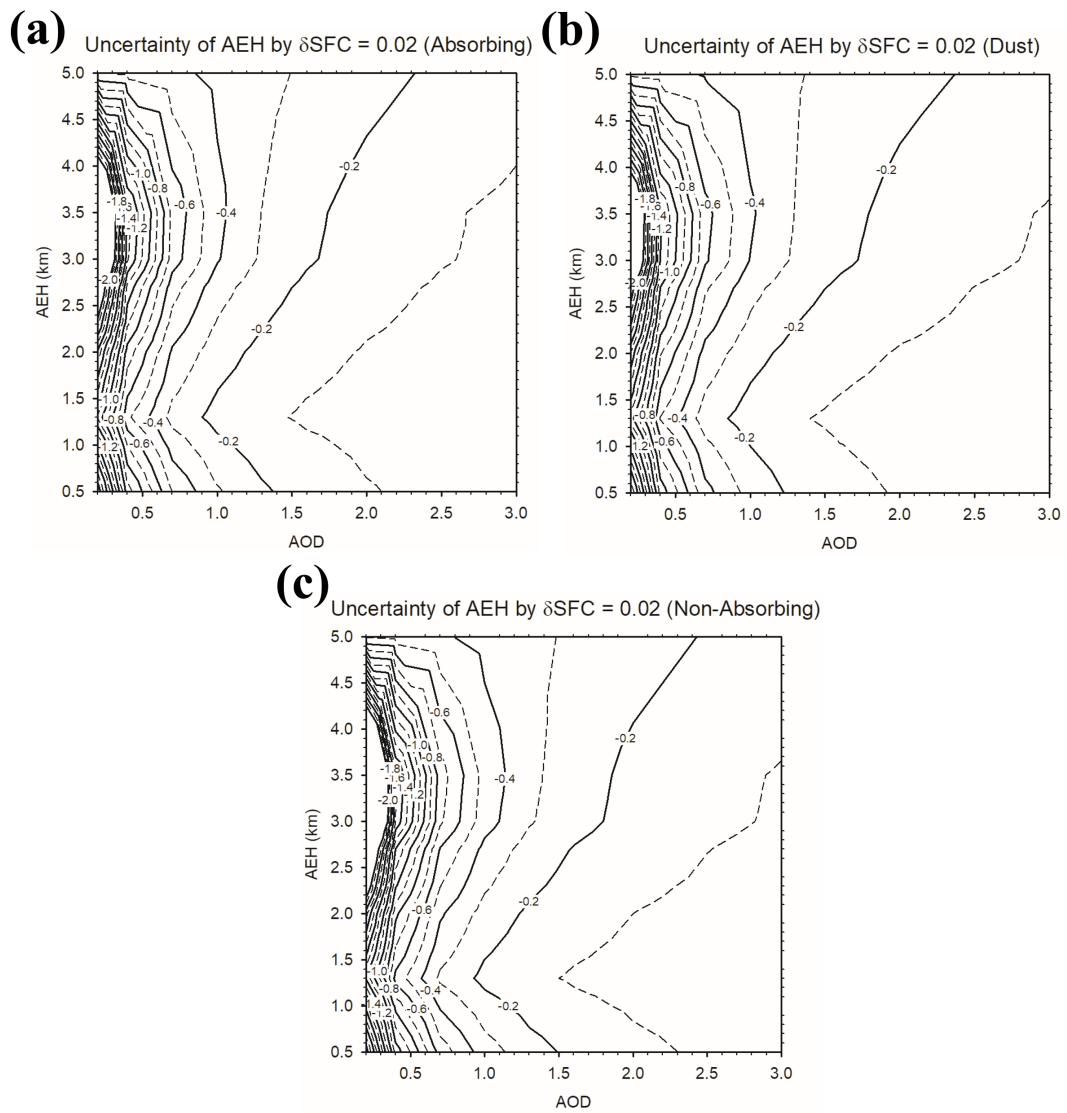389   Absorbing, (b) Dust, and (c) Non-Absorbing aerosol types.

(a) Uncertainty of AEH by δSFC = 0.02 (Absorbing)

(b) Uncertainty of AEH by δSFC = 0.02 (Dust)

(c) Uncertainty of AEH by δSFC = 0.02 (Non-Absorbing)

390

391   **Figure 5.** AEH retrieval uncertainty by the surface reflectance error of 0.02 according

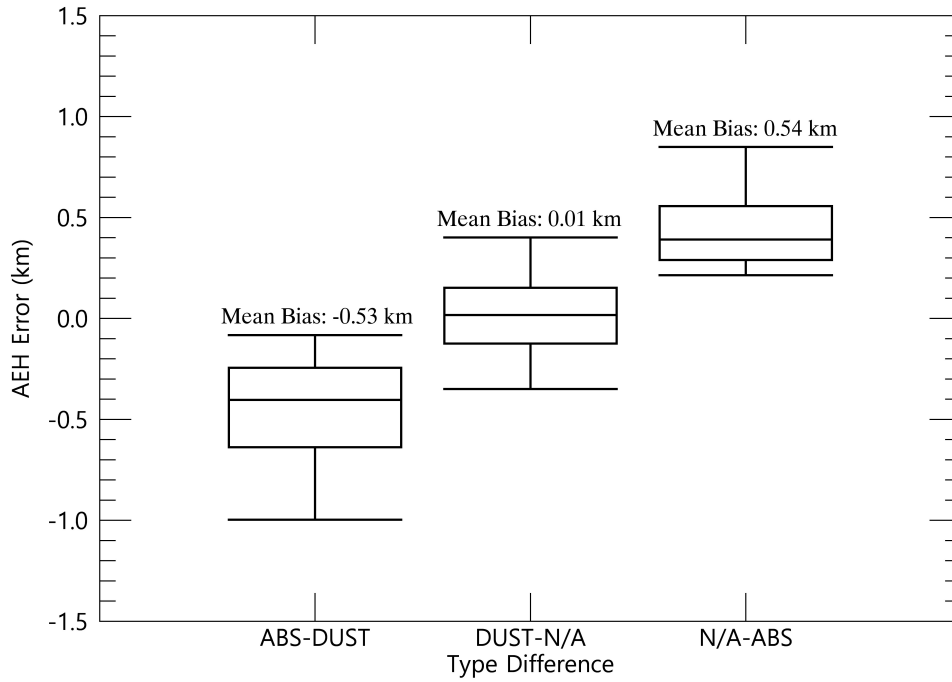392   to (a) Absorbing, (b) Dust, and (c) Non-Absorbing aerosol types.

393

Figure 6. AEH retrieval uncertainty caused by the aerosol type misclassification.

Figure 6 shows the retrieval uncertainty caused by misclassification of the aerosol types. On average, the AEH retrieval uncertainty has an impact of up to 0.5 km, but this uncertainty shows larger than 2 km uncertainty under low AOD and short optical path length conditions. Based on the changes in sensitivity observed for optical path length, aerosol type (in terms of SSA) and AOD, and surface reflectance are carefully considered as input parameters for AEH retrieval. In the AEH retrieval, the AOD, aerosol type, and SSA are obtained from the L2AERAOD, which is standard aerosol product of GEMS. As shown in Section 2.1, the L2SFC product is used in operation, but this study used the climatological minimum Lambertian surface reflectance. However, the aerosol vertical distribution is always fixed as GDF function profiles as shown in Spurr and Christi (2014). The data quality of AEH retrieval results are considered the qualities of aerosol optical property and DOAS fitting results.

23

4. Case studies

Figure 7 shows retrieval results for AEH from GEMS on March 29 over East Asia. Because the operational schedule is hourly during the daytime, the GEMS retrieval results are shown at 1-hour intervals from 01:00 to 07:00 Universal Time Coordinated (UTC). AOD and SSA are also shown in Figures S1 and S2, respectively. From Park et al. (2016), pixels with low AOD values have large AEH uncertainty due to weak aerosol scattering information. For this reason, only AEH retrieval results with AOD greater than 0.3 are shown in this study. In addition, the AEH retrieval results are also adopted to the quality flag for "Reliable" from L2AERAOD, which considers the significant averaging kernel for optimal estimation for aerosol property retrievals. During this case study, a dust plume was located along the coast of China and South Korea with AOD at 443 nm of 0.8~1.2. Simultaneously, another plume was also present over the northeastern Korean Peninsula with AOD of 1.0~2.0 at 443 nm. SSA at 443 nm was 0.90~0.93 for the plume over South Korea and 0.87~0.90 for the plume over the northeastern Korean Peninsula. Retrieved AEH results from these different plumes show similar ranges. For both detected plumes, the AEH shows similar pattern ranging between 1.0 to 2.0 km in this case.
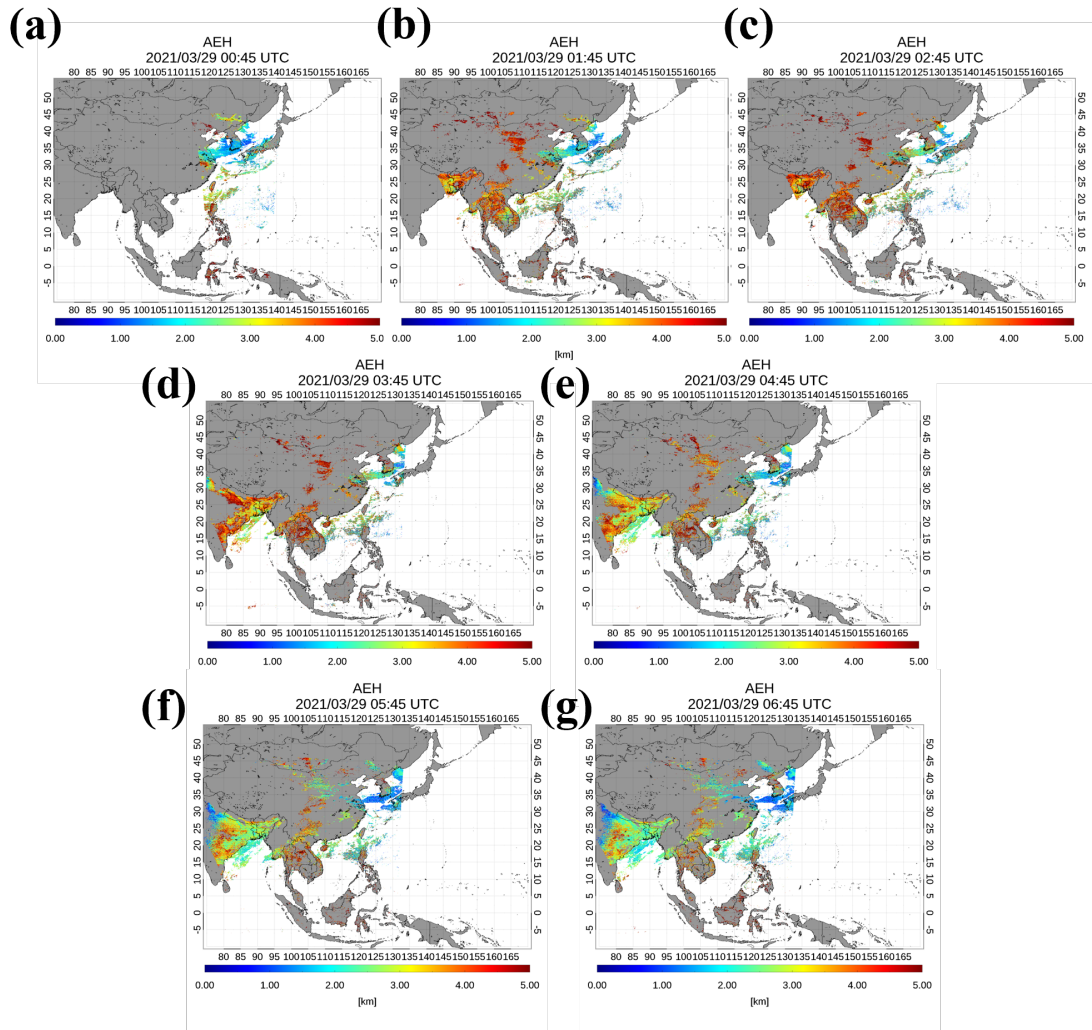
Figure 7. Case study results for AEH based on GEMS observations on March 29, 2021 [(a) 00:45 UTC, (b) 01:45 UTC, (c) 02:45 UTC, (d) 03:45 UTC, (e) 04:45 UTC, (f) 05:45 UTC, and (g) 06:45 UTC].

An additional severe aerosol plume was present over northeastern India, with AOD at 443 nm of 1.0~2.0 and SSA at 443 nm of 0.85~0.90. From Rana *et al.* (2019), metropolitan cities and industrial cluster in India are heavy emitters of black carbon, and high concentrations of black carbon are distributed over the Indo-Gangetic Plain (IGP). Therefore, the aerosol plume with high AOD and low SSA (high absorbing) was a result that actually exists, and it was not a result with high uncertainty due to edge of GEMS

observation field. Except for the inland parts of India, AEH in high AOD pixels ranged
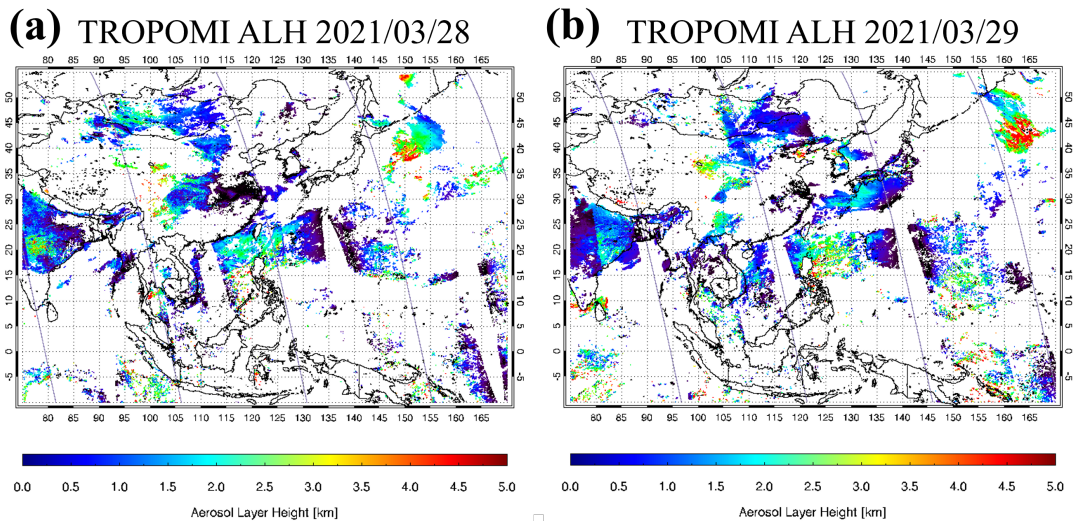
from 1.5 to 3.5 km.

Figure 8. ALH retrieved from TROPOMI and orbit path of CALIOP on (a) March 28 and (b) March 29, 2021 (Unit: km).

For comparison of the retrieval, Figure 8 shows the ALH retrieved from TROPOMI on March 28 and 29, 2021 over East Asia. A dust plume was transported from China to South Korea during this period, then split into two distinct plumes over northeastern China and the coastal area of South Korea. The ALH retrieved from TROPOMI for both plumes were 0.5~1.5 km. Given the difference in definition for the aerosol height parameters between ALH and AEH, relatively high height values were retrieved from GEMS compared to TROPOMI. In an ideal case under symmetric gaussian distribution with a width of 1 km, the AEH from GEMS was around 0.5 km higher than the peak height of aerosol layer. The ALH expresses the center (or peak) height, thus, the AEH from GEMS was overestimated by around 0.5 km relative to the ALH from TROPOMI. Although AEH had higher values than ALH from TROPOMI, the GEMS AEH retrievals for the dust transport case study were successfully retrieved.
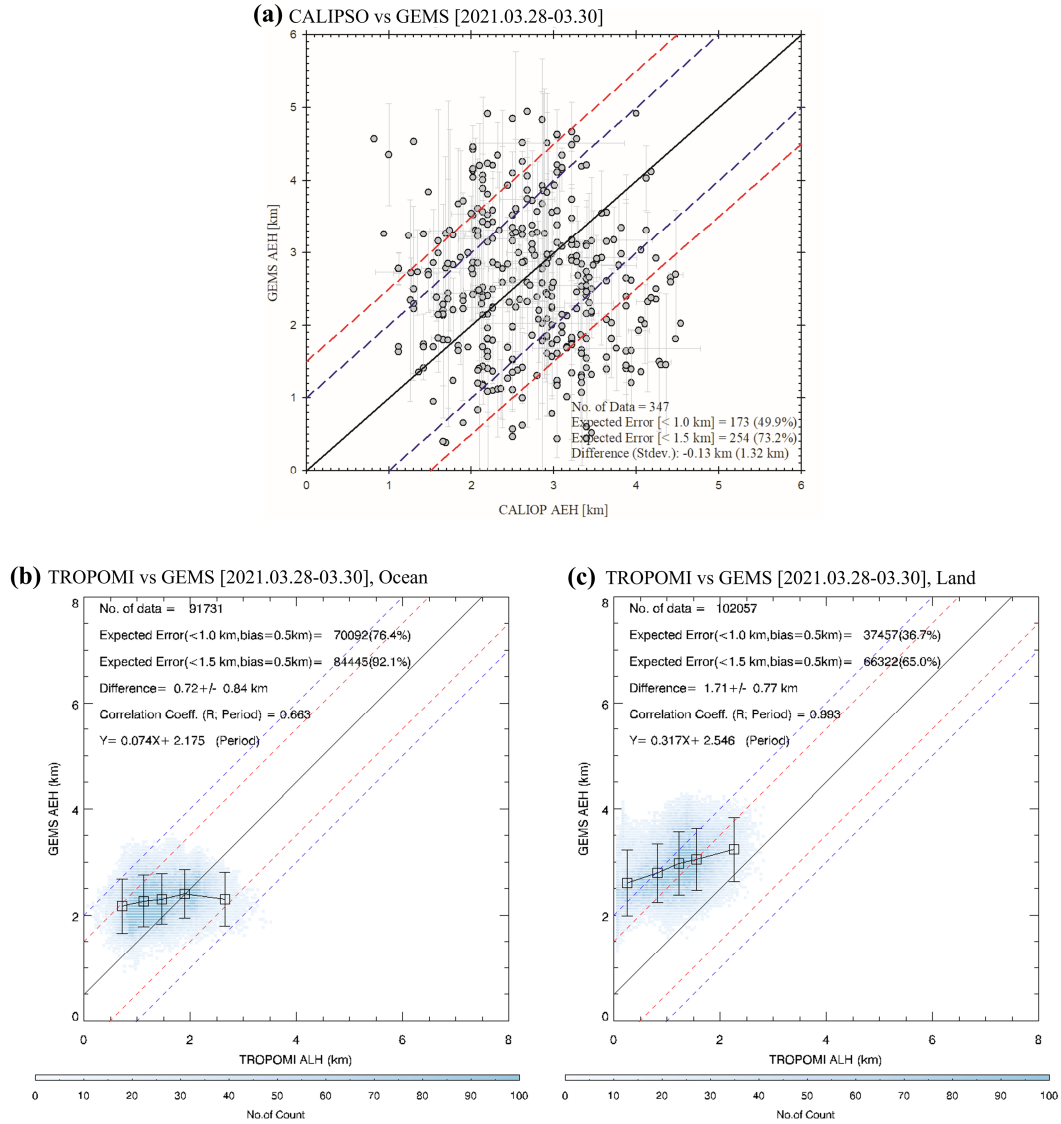
26

(a) CALIPSO vs GEMS [2021.03.28-03.30]

No. of Data = 347
Expected Error [< 1.0 km] = 173 (49.9%)
Expected Error [< 1.5 km] = 254 (73.2%)
Difference (Stdev.): -0.13 km (1.32 km)

(b) TROPOMI vs GEMS [2021.03.28-03.30], Ocean

No. of data = 91731
Expected Error(<1.0 km,bias=0.5km)= 70092(76.4%)
Expected Error(<1.5 km,bias=0.5km)= 84445(92.1%)
Difference= 0.72+/- 0.84 km
Correlation Coeff. (R; Period) = 0.663
Y= 0.074X+ 2.175 (Period)

(c) TROPOMI vs GEMS [2021.03.28-03.30], Land

No. of data = 102057
Expected Error(<1.0 km,bias=0.5km)= 37457(36.7%)
Expected Error(<1.5 km,bias=0.5km)= 66322(65.0%)
Difference= 1.71+/- 0.77 km
Correlation Coeff. (R; Period) = 0.893
Y= 0.317X+ 2.546 (Period)

Figure 9. Intercomparison of (a) AEH between CALIOP and GEMS and (b) ALH from TROPOMI and AEH from GEMS over ocean and (c) over land (Black box and error bar is mean and standard deviation in 20% interval of each TROPOMI ALH) over the period from March 28 to 30, 2021.

Figure 9 shows intercomparison results for aerosol plume height among GEMS, CALIOP, and TROPOMI during the case study of dust transport in East Asia from March 28 to 30, 2021. For the direct comparison shown in Figure 9a, the difference in AEH between GEMS and CALIOP was -0.13±1.32 km. Nanda *et al.* (2020) reported

461 that the difference in ALH between TROPOMI and CALIOP was 0.53 km for 4 cases of

462 thick Saharan dust plumes. In addition, 49.9% and 73.2% of the total pixels showed

463 differences less than 1.0 and 1.5 km, respectively. Large AEH uncertainty occurred

464 mostly over the inland area of China. Because AEH from GEMS uses only the O_2-O_2

465 absorption band, the accuracy of AEH is sensitive to uncertainty in surface reflectance

466 and AOD. From Park et al. (2016), total error budget of AEH is 0.74~1.28 km, and the

467 total error budget considered the uncertainty of AOD, SSA, aerosol particle size, and

468 surface albedo in the aerosol retrieval process. The total error budget amount from the

469 previous study is similar value of standard deviation of AEH difference between GEMS

470 and CALIOP.

471 Figures 9b and 9c illustrate the comparison results between GEMS AEH and

472 TROPOMI ALH, for the period of March 28~30, 2021 over land and ocean surface,

473 respectively. The difference between GEMS AEH and TROPOMI ALH was 0.72 ± 0.84

474 km and 1.71 ± 0.77 km over ocean and land in this case, respectively. In addition, 82.4%

475 and 37.3% of all pixels had differences less than 1.5 km over ocean and land,

476 respectively. However, the ALH from TROPOMI is generally lower than the AEH from

477 GEMS because of the discrepancy in definitions. Based on the assumption of aerosol

478 vertical distribution for AEH retrieval, the difference between AEH and center height of

479 aerosol extinction profile is around 0.5 km. To consider the inconsistency of definition

480 between ALH and AEH, the difference between two retrieval results decreased to 0.5

481 km bias. After consideration of definition inconsistency, the proportion of pixels within

482 the expected error ranges of 1.5 km are enhanced to 92.1% and 65.0% over ocean and
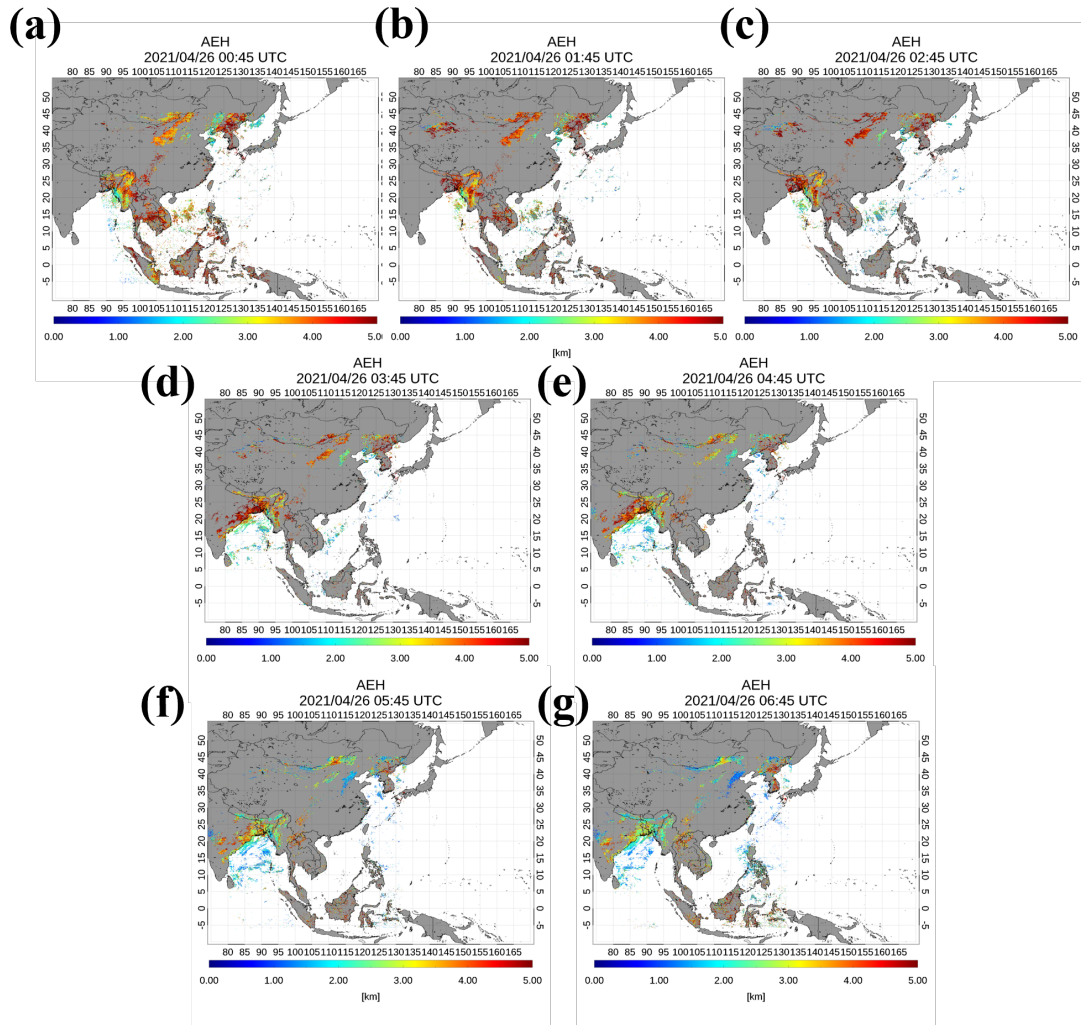
483 land, respectively.

Figure 10. Case study results for AEH based on GEMS observations on April 26, 2021 [(a) 00:45 UTC, (b) 01:45 UTC, (c) 02:45 UTC, (d) 03:45 UTC, (e) 04:45 UTC, (f) 05:45 UTC, and (g) 06:45 UTC].

484

485

486

487

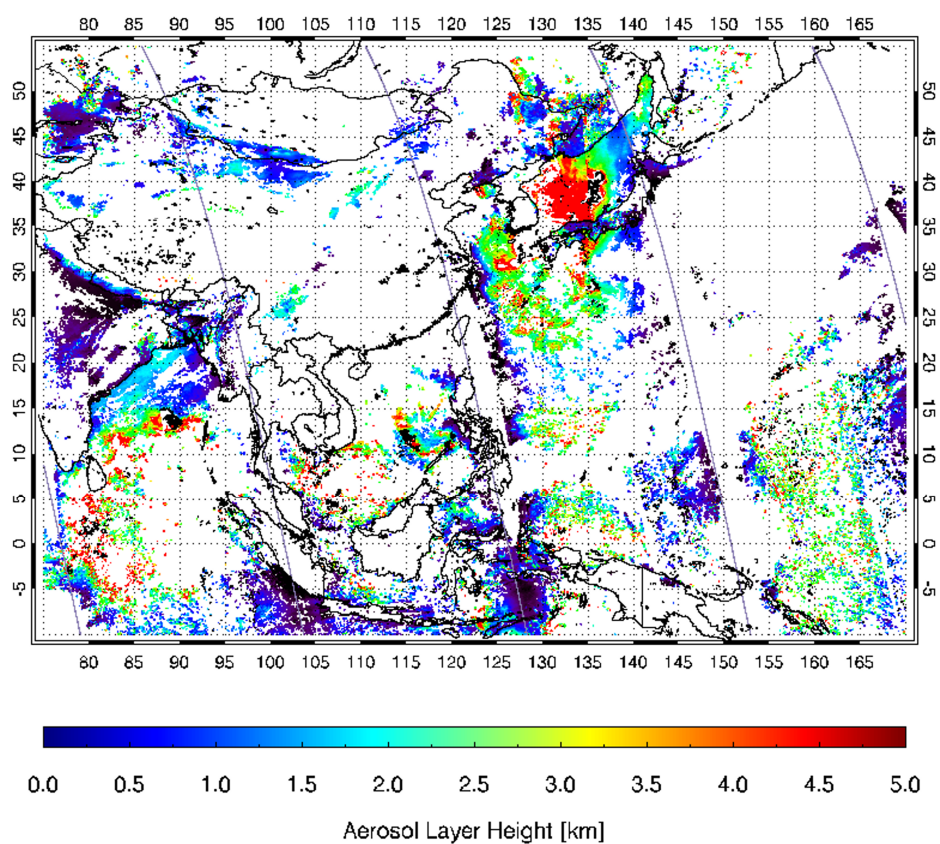TROPOMI ALH 2021/04/26

488

Figure 11. ALH retrieved from TROPOMI and orbit path of CALIOP on April 26,
2021 (Unit: km).

(a) CALIPSO vs GEMS [2021.04.26]

No. of Data = 83
Expected Error [< 1.0 km] = 63 (75.9%)
Expected Error [< 1.5 km] = 72 (86.7%)
Difference (Stdev.): -0.15 km (0.97 km)

(b) TROPOMI vs GEMS [2021.04.26], Ocean

No. of data = 9873
Expected Error(<1.0 km,bias=0.5km)= 6426(65.1%)
Expected Error(<1.5 km,bias=0.5km)= 7727(78.3%)
Difference= -0.14+/- 1.08 km
Correlation Coeff. (R; Period) = 0.657
Y= 0.123X+ 1.546 (Period)

(c) TROPOMI vs GEMS [2021.04.26], Land

No. of data = 15344
Expected Error(<1.0 km,bias=0.5km)= 6527(42.5%)
Expected Error(<1.5 km,bias=0.5km)= 9970(65.0%)
Difference= 1.47+/- 1.09 km
Correlation Coeff. (R; Period) = 0.810
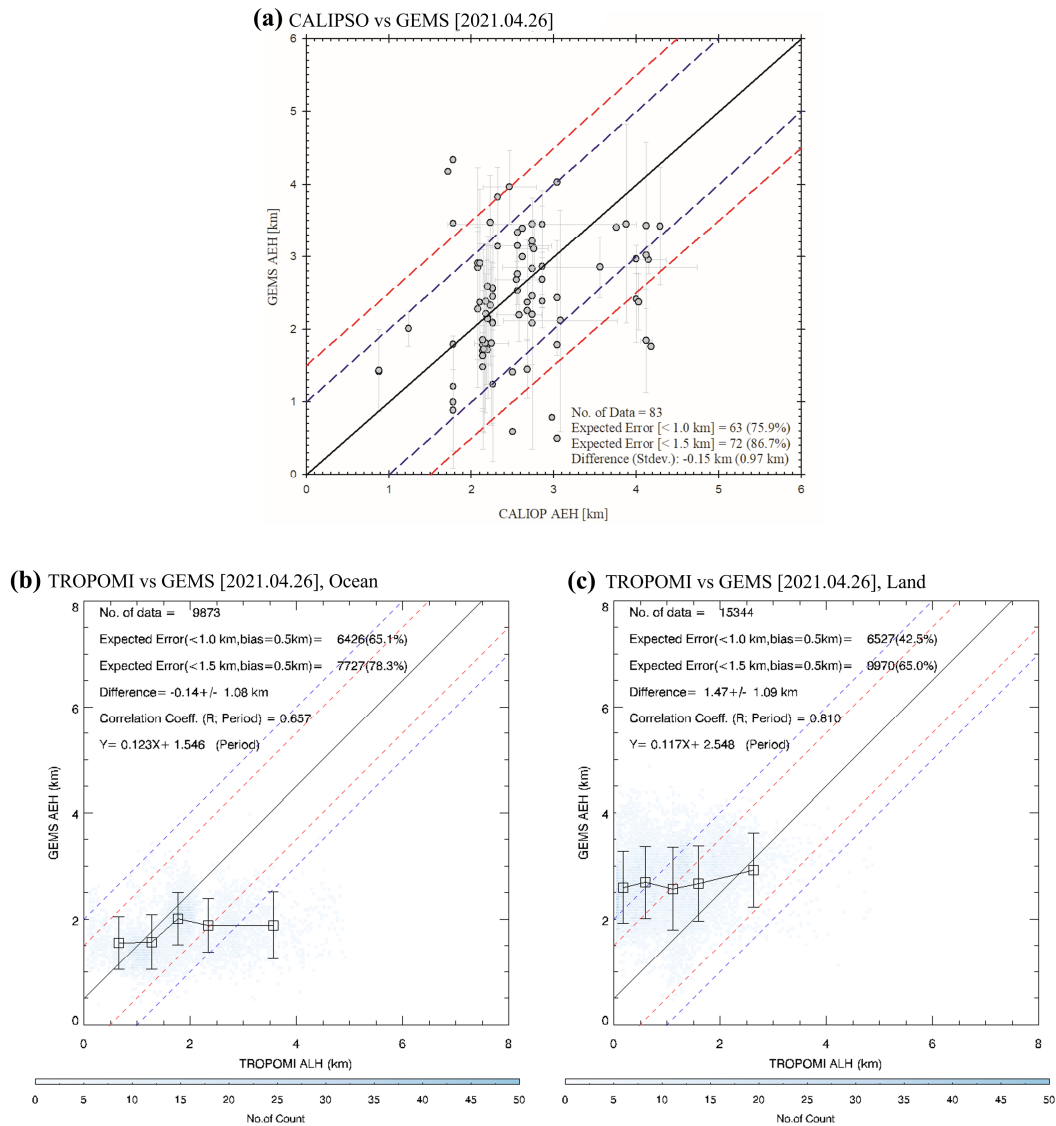Y= 0.117X+ 2.548 (Period)

Figure 12. Intercomparison of (a) AEH between CALIOP and GEMS, and (b) ALH from TROPOMI and AEH from GEMS over ocean and (c) over land (black dot and error bar is mean and standard deviation in 20% interval of each TROPOMI ALH) on April 26, 2021.

An additional intercomparison case of April 26, 2021, is shown in Figures 10 (GEMS) and 11 (TROPOMI). During the transport of the dust plume from inland China to the coastal area, AEH changed from 4.0 km at 02:00 UTC to 2.0 km at 06:00 UTC. By contrast, ALH from TROPOMI only observed the 1.5~2.5 km layer height over East

500   Asia around 04:00 UTC. Although the AEH from GEMS had spatio-temporal

501   uncertainty, this case demonstrates the advantage of AEH retrieval from GEMS for

502   continuous monitoring of changes in plume height, in particular during dust transport.

503   As shown in Figure 12, AEH from GEMS showed differences in height of -0.15 ± 0.97

504   km (compared to CALIOP). In addition, the differences in height of -0.14 ± 1.06 and

505   1.47 ± 1.09 km over ocean and land as compared to TROPOMI ALH.

506   From two different case results, proportion values within 1.0 km (or 1.5 km) height

507   difference between TROPOMI and GEMS have strong dependence of surface types.

508   The proportion over land (over ocean) was lower (higher) than the corresponding result

509   from the comparison of GEMS and CALIOP. The TROPOMI ALH from version 2 is

510   strong surface type dependence as compared to the ground lidar data (Michailidis et al.,

511   2023). However, the relationship between TROPOMI ALH and GEMS AEH in 20%

512   interval of each TROPOMI ALH have high correlation coefficients. In the case of

513   March 28~30, the correlation coefficients between TROPOMI and GEMS are 0.663 and

514   0.993 over ocean and land, respectively. In the case of April 26, the correlation

515   coefficients are 0.657 and 0.810 over ocean and land, respectively.

516

517   **5. Long-term validation**

518   For long-term validation, we used the AEH retrieval results from January to June,

519   2021. The CALIOP and TROPOMI satellites passed over the study area around 13:30

520   local time, which is around 04:30 UTC for East Asia and around 06:30 UTC for India.

521   Most temporal colocation pixels aligned with observation times of 04:00~06:00 UTC,

522   respectively. To check the dependence of several retrieval variables, the UVAI, AOD,

523   SSA, and dominant aerosol type in each pixel (TYPE) were obtained from the

524   L2AERAOD. Although the GEMS algorithm retrieved AEH in the range of 0~10 km,

525   the sensitivity of O_2-O_2 SCD was weak in cases of high AEH because of the vertical

526   distribution of air molecules. To ensure sufficient quality of retrieved data, therefore, the

527   AEHs from GEMS and CALIOP, and the ALH from TROPOMI were used only in

528   pixels where the AEH from GEMS were lower than 5 km.
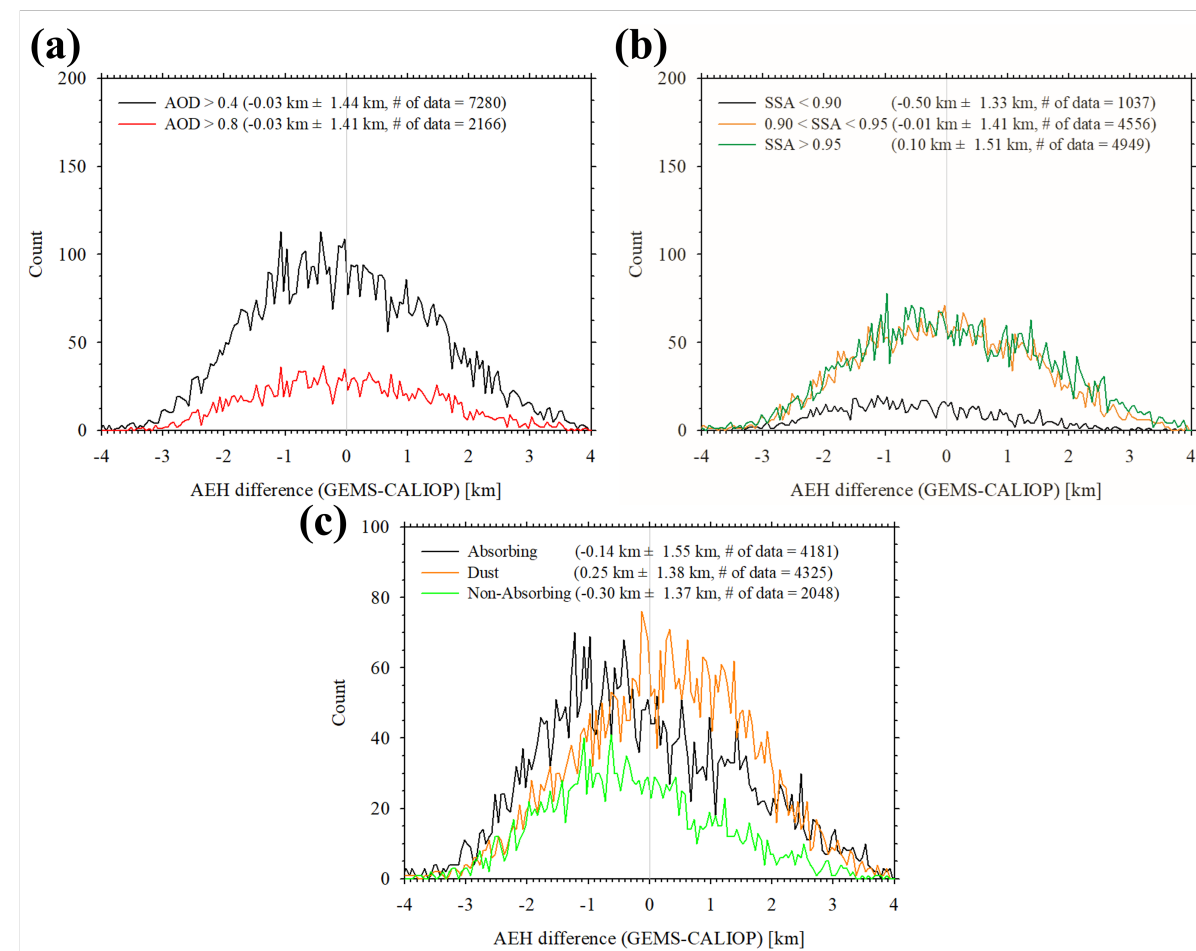
529

530

531   **Figure 13.** Histogram of AEH difference between CALIOP and GEMS with respect

532   to (a) AOD, (b) SSA, and (c) TYPE from GEMS over the period from January 1 to June

533   30, 2021.

534

535   Figure 13 shows histograms of difference in AEH between GEMS and CALIOP

536   according to AOD at 443 nm, SSA at 443 nm, and TYPE from GEMS. From Figure 13a,

537   the dependence on AOD threshold was insignificant; the average estimated AEH

538   difference was -0.03 km, but the variation in AEH difference was around 1.4 km based

539   on the standard deviation for AOD > 0.4. Because of uncertainty in GEMS aerosol

540   operational products, AEH from GEMS exhibits large variability. Although

541   L2AERAOD from GEMS retrieved the AOD, SSA, and aerosol types, the retrieved

542   results from L2AERAOD include significant uncertainty. Go et al. (2020) reported that

543   the root-mean square error (RMSE) of AOD between MODIS and OMI UV aerosol

544   algorithm is 0.276~0.341.

545   In addition, fitting error perturbs the fitting signals and tends to result in the

546   underestimation of SCD. Although the fitting error of O_2-O_2 SCD from GEMS radiance

547   was minimized, the fitting error has still remained around 6%, as indicated in Table 2.

548   The discrepancy in fitting condition between the simulated and observed radiance

549   biased the SCD estimation, which in turn led to bias and variation in the AEH retrieval.

550   Combined with the high sensitivity of AEH errors to aerosol optical properties,

551   uncertainty arising from L2AERAOD causes AEH variability.

552   The variation in AEH difference between observation platforms is shown in Figure

553   13b as a histogram according to SSA threshold. Across the entire SSA threshold range,

554   the standard deviation of the AEH difference was 1.33~1.51 km. In particular, this

555   standard deviation decreased slightly with decreasing SSA. The aerosol height

556   parameter is more sensitive to absorbing-dominant aerosols than scattering-dominant

557   aerosols (e.g., Park et al., 2016; Nanda et al., 2020). For this reason, the variability of

558   AEH is smaller in absorbing-dominant aerosols than scattering-dominant aerosols, if the

34

559 uncertainty of other aerosol parameters (AOD, SSA, and TYPE) is the same conditions.

560 Figure 13c shows the dependence of AEH difference on TYPE. The TYPE product

561 included dependence on the aerosol size and optical absorptivity. For this reason, the

562 AEH difference graphs for the "Dust" and "Absorbing" types differ, despite both types

563 being absorbing-dominant aerosols. The AEH difference for the "Absorbing" type

564 showed a negative bias with a large standard deviation, whereas a positive bias with a

565 small standard deviation was obtained for the "Dust" type. The AEH difference for the

566 "Non-Absorbing" aerosol type showed the largest negative bias in this comparison.

567 These results suggest that the aerosol size distribution of fine particles affects the

568 negative bias of AEH. Combined with the AEH difference bias illustrated in Figure 8b,

569 these findings indicate that the bias in AEH difference for "Absorbing" aerosols is

570 weakened by their absorbing-dominant property.

571 Figure 14 shows means and standard deviations for AEH difference between

572 CALIOP and GEMS according to AOD and AI values from GEMS. For AOD, the mean

573 AEH difference ranged from -0.13 to 0.03 km with a standard deviation of

574 approximately 1.45 km. Similar to Figure 13a, the variation in AEH difference with

575 AOD change was insignificant. For the AI, the lowest AEH difference was -0.19 km,

576 obtained for the AI range of 1.5~2.0. The largest AEH difference was 0.24 km for the AI

577 range of 4.0~4.5. Although the AEH difference varied slightly, no consistent tendency in

578 AEH variation with AI was observed. Overall, the standard deviation of AEH difference

579 ranged from 1.49 km (0.0 < AI < 0.5) to 1.18 km (4.5 < AI < 5.0), and a consistent

580 tendency of decreasing variance in AEH difference was found with increasing AI.
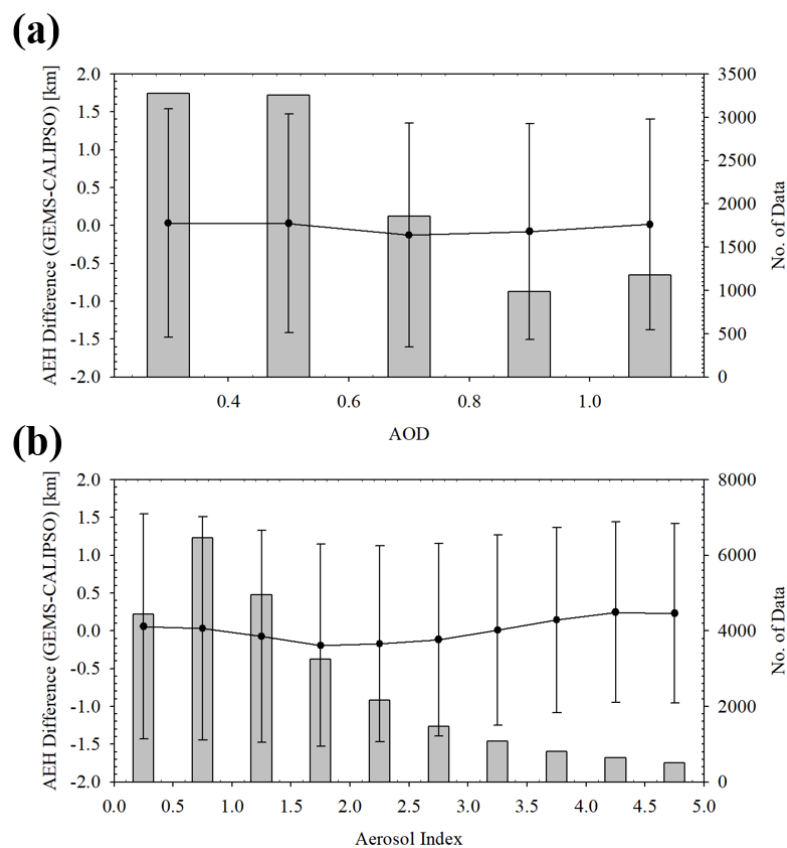
Figure 14. AEH difference between CALIOP and GEMS with respect to ranges of (a) AOD and (b) AI obtained from GEMS from January 1 to June 30, 2021 (Black dots and error bars denote the mean and standard deviation of AEH difference, while the gray-box indicates the number of data).
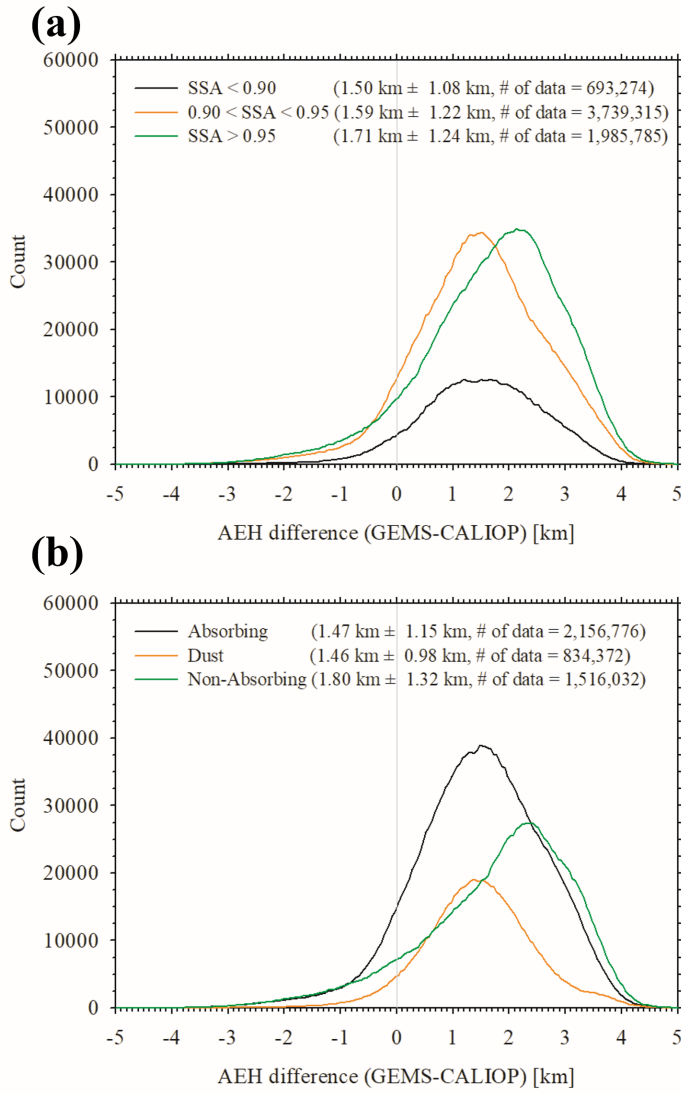
(a)

(b)

Figure 15. Histograms of differences between TROPOMI ALH and GEMS AEH
with respect to (a) SSA, and (b) TYPE from GEMS in the period from January 1 to June
30, 2021.

Figure 15 shows histograms of differences between GEMS AEH and TROPOMI
ALH according to the SSA and TYPE obtained from GEMS. The difference between
GEMS AEH and TROPOMI ALH depends on both SSA and TYPE. The mean
difference value between GEMS AEH and TROPOMI ALH decreased as the aerosol

37

absorptivity increased. This difference was 1.50 ± 1.08, 1.59 ± 1.22, and 1.71 ± 1.24 km for pixels of SSA < 0.90, 0.90 < SSA < 0.95, and SSA > 0.95, respectively. Comparing these results to Figure 13b, we find that the standard deviation of the comparison with TROPOMI was approximately 75% of the corresponding value for CALIOP. It is because both TROPOMI and GEMS are passive sensors that use similar retrieval methods for oxygen absorption bands. Nanda *et al.* (2020) showed that the operational algorithm of TROPOMI operational algorithm can provide ALH pixel retrievals only for scenes dominated by absorbing aerosol particles. In addition, Griffin *et al.* (2020) reported that the pixels with low positive UVAI values (weak absorbing cases) are identified with low QA values (QA ≤ 0.5) in the offline product of ALH. Although the TROPOMI ALH algorithm updated for the expansion of retrieval range, the contrast of O_2-O_2 SCD to the aerosol layer height change is fundamentally weak sensitivity in scattering dominant aerosols (e.g., Park et al., 2016). For this reason, the bias and standard deviation of height difference between GEMS and ALH is generally larger in high SSA.

In addition, difference between GEMS AEH and TROPOMI ALH depends on TYPE, as shown in Figure 15b. The difference was 1.47 ± 1.15, 1.46 ± 0.98, and 1.80 ± 1.32 km for "Absorbing", "Dust", and "Non-Absorbing" type aerosols, respectively. Similar to Figure 13c, the TYPE dependence of aerosol height information was influenced by both absorptivity and size information. In addition, the difference in the definition of ALH from TROPOMI and AEH from GEMS impacted the comparison. "Dust" type of aerosol is mainly transported in the free troposphere with gaussian-like vertical distribution, and the associated plume thickness is highly variable. However, "Absorbing" aerosols mainly originate from anthropogenic emissions in East Asia and

38

620   mostly distributed near the surface with homogeneous concentration (e.g., Gao *et al.*,

621   2014; Wang *et al.*, 2012; Peng *et al.*, 2016). Transport patterns and vertical distribution

622   shape depending on aerosol types, can affect the accuracy of aerosol height retrieval
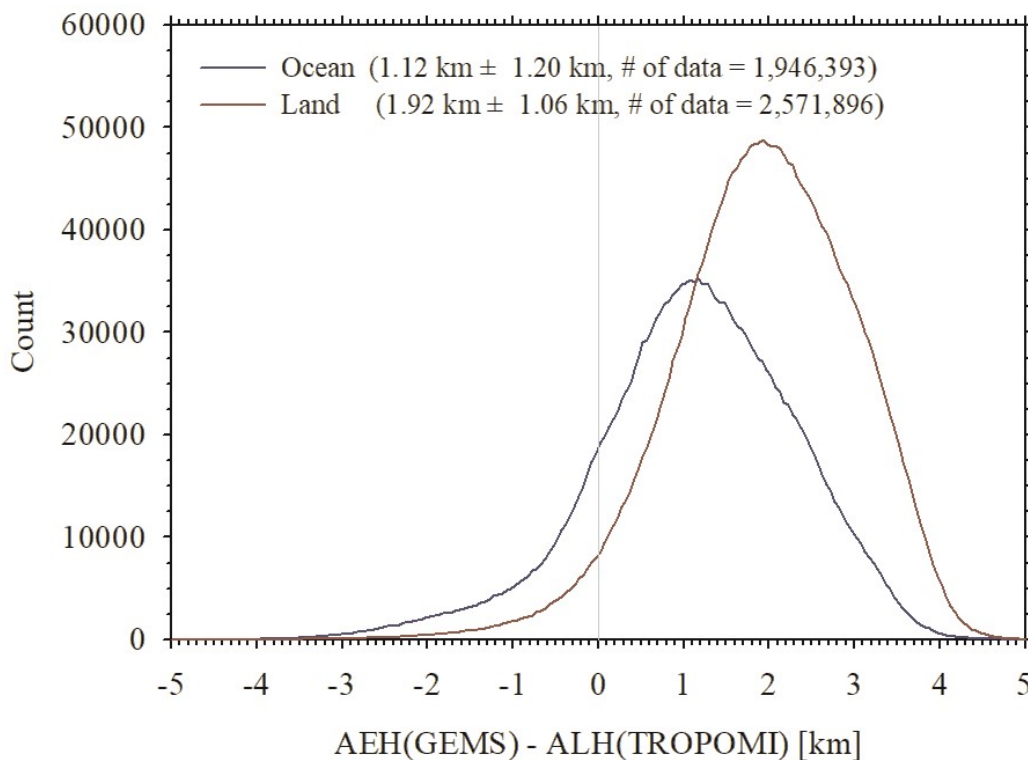
623   results.

624

625   **Figure 16.** Histogram of the difference between TROPOMI ALH and GEMS AEH

626   over land and ocean pixels, respectively, from January 1 to June 30, 2021.

627

628   The non-Lambertian effect on the land surface impacted surface albedo uncertainty

629   during AEH retrieval, and this effect led to bias and variance in AEH. In this study, the

630   minimum Lambertian equivalent reflectance was used as the reference reflectance value.

631   However, surface reflectivity has geometric dependence due to non-Lambertian effects,

632   which leads to a bias of 0.01-0.02 for surface reflectance over the land surface (e.g., Qin

633   *et al.*, 2019). To identify the sensitivity of surface property, a histogram was constructed

634   of difference between GEMS AEH and TROPOMI ALH after classification into land

635   and ocean surface types, as shown in Figure 16. From the statistical results, the mean

636   differences were estimated to be 1.12 ± 1.20 and 1.92 ± 1.06 km for ocean and land

637   pixels, respectively. The bias has significant difference between two different surface

638   types. Michailidis et al. (2023) explained that the experimental retrieval range of ALH

639   from TROPOMI is 0.27~6.5 km and 0.06~2.15 km over ocean and land, respectively.

640   Constrained retrieval range over land by the TROPOMI influences the negative bias of

641   aerosol height retrieval and increases the mean difference of aerosol height between

642   GEMS and TROPOMI. In addition, the non-Lambertian effect for surface reflectance is

643   also affecting the increasing the discrepancy of aerosol height information. ~~indicating~~

644   ~~insignificant difference in bias between these two surface covers. However, the standard~~

645   ~~deviation of the two surface types indicated a significant difference. Over the ocean~~

646   ~~surface, the histogram is very narrow. Although there are 6.5 times more data for land~~

647   ~~than those for the ocean surface, the land surface has a relatively wide histogram~~

648   ~~distribution. This discrepancy arises because the non-Lambertian effect causes bias in~~

649   ~~surface reflectance, while also influencing the variability in surface reflectance related~~

650   ~~to observation geometry. For this reason, land surface reflectance based on the non-~~

651   ~~Lambertian surface assumption is not fully representative of actual surface reflectance~~

652   ~~as a function of observation geometry. Therefore, the standard deviation of the layer~~

653   ~~height difference is larger over the land surface, and the significant difference between~~

654   ~~land and ocean pixels is mainly driven by the assumption of surface reflection~~
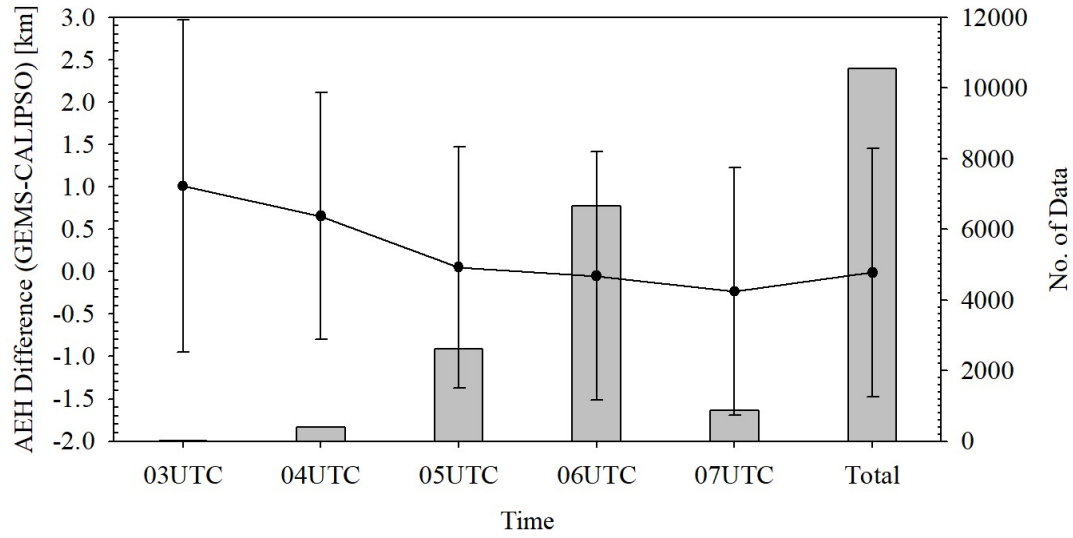
655   ~~properties.~~

656

657

Figure 17. Diurnal dependence of AEH difference between CALIOP and GEMS
from January 1 to June 30, 2021 (Black dots and error bars denote the mean and
standard deviation of AEH difference, while the gray-box indicates the number of data).

The results of hourly statistical analyses are presented in Figure 17. Because they use
a consistent definition of AEH, we show only a comparison of GEMS and CALIOP. The
diurnal variation in AEH difference ranged from -0.23 ± 1.45 km (07:00 UTC, Number
of Data = 867) to 1.01 ± 1.96 km (03:00 UTC, Number of Data = 23). However, the
number of pixels observed at 03:00 UTC was insufficient for the identification of
diurnal variation. The AEH difference of 0.66 ± 1.45 km was the next highest value
obtained at 04:00 UTC (Number of Data = 395). The inhomogeneous number of data is
mainly due to the lack of spatial homogeneity among retrieval pixels. Over India, very
high AOD values were consistently observed during the comparison period. Otherwise,
the AEH was only retrieved under conditions of severe anthropogenic emissions over
East Asia. In addition, the diurnal variation in AEH difference was caused by spatial

673   characteristics of AEH difference. From 03:00 to 05:00 UTC, CALIOP mainly passed

674   over East Asia, which has numerous sources of aerosol emissions, including biomass

675   burning, dust, and industrial activity. In addition, GEMS observed only the eastern part

676   of India, which is dominated by anthropogenic aerosols. The spatial distribution of the

677   dominant aerosol types may impact the diurnal variation in AEH difference.

678

6. Summary & Conclusions

680   Based on the possibility of retrieving AEH from environmental satellite sensors, an

681   AEH retrieval algorithm for GEMS was developed that solely uses the O_2-O_2 absorption

682   band with considering aerosol and surface properties. Because the sensitivity of AEH

683   retrieval is strongly affected by optical amounts and properties of aerosols, as well as

684   surface reflectivity, an AEH retrieval algorithm for GEMS was developed after retrieval

685   of the GEMS operational algorithms, L2AERAOD and L2SFC. With the newly

686   developed retrieval algorithm, GEMS can be used to monitor aerosol vertical

687   information with high temporal and spatial resolution. ~~To ensure the sensitivity of AEH~~

688   ~~retrieval, only AEH retrieval results are with AOD larger than 0.3 were shown.~~

689   For dust plumes over East Asia, AEH retrieval results from GEMS indicated

690   appropriated aerosol vertical information. After spatial and temporal colocation, the

691   AEH from GEMS aligned well with the AEH information obtained from CALIOP. The

692   differences in AEH between GEMS and CALIOP for dust plume cases were -0.13 ±

693   1.32 and -0.15 ± 0.97 km, with 49.9~75.9% and 73.2~86.7% of all pixels showing

694   differences less than 1.0 and 1.5 km, respectively. Large AEH uncertainty was found

695   mostly over inland China due to uncertainty in surface reflectance and AOD over the

696   land surface. In addition, AEH from GEMS was overestimated compared to the

697   TROPOMI ALH results. The overestimation is partially caused by different definitions

698   of ALH from TROPOMI and AEH from GEMS.

699   In long-term intercomparison with CALIOP, the average AEH difference was

700   estimated to be -0.03 km, with a standard deviation of 1.4 km under the scenario of

701   AOD > 0.4. ~~In terms of sensitivity to surface types, the mean differences were estimated~~

702   ~~to be 1.12 and 1.92 km over the ocean and land, respectively.~~ The large variation in

703   AEH difference between GEMS and CALIOP was caused by uncertainty in the input

704   parameters estimated from L2AERAOD and L2SFC. In the long-term intercomparison

705   against TROPOMI, this difference was dependent on both SSA and TYPE. The

706   difference was 1.50 ± 1.08 km, 1.59 ± 1.22 km, and 1.71 ± 1.24 km for pixels with SSA

707   < 0.90, 0.90 < SSA < 0.95, and SSA > 0.95, respectively. In addition, differences of 1.47

708   $\pm$ 1.15 km, 1.46 ± 0.98 km, and 1.80 ± 1.32 km were obtained for the "Absorbing",

709   "Dust", and the "Non-Absorbing" types of aerosols, respectively. The AEH difference

710   also has a diurnal dependence, which is ranged from -0.23 ± 1.45 km to 1.01 ± 1.96 km,

711   due to the spatial characteristics of dominant aerosol types.

712   The case studies and results of the long-term validation show that AEH retrieved

713   from GEMS can provide information on aerosol vertical distribution, with applications

714   in diverse research fields. The AEH results with the long-term statistical accuracy make

715   possible to use the application study for AMF calculation of GEMS trace gas retrieval.

716   In addition, AEH considerably affects the surface particulate matter (PM) concentration

717   obtained from satellite-based AOD because PM estimation is significantly affected by

718   the mixing layer height of aerosols. For this reason, the AEH can provide the effective

719   mixing layer height of aerosols for anthropogenic aerosols, and also provide the vertical

720   patterns for long-range transport of aerosols.

721   Although several fields of study may apply the AEH retrieval results, retrieval

722   uncertainty in AEH remains due to the uncertainty of retrieved AOD and SSA. In

723   addition, the uncertainty in surface reflectance and the discrepancy in O_2-O_2 SCD

724   values between the simulation results and observations can be affected to the potential

725   error sources of AEH from GEMS. To minimize the AEH retrieval uncertainty, further

726   analysis related to the optimized input parameters of AOD, SSA, and aerosol type

727   information is essential. For this reason, the quantitative analysis AEH uncertainty due

728   to aerosol and surface property is important for the improvement of AEH retrieval

729   algorithm. In addition, aerosol optical property retrieval by the visible channel will be

730   needed for the further study to improve the aerosol type determination. Although the

731   aerosol indices of UV and visible provide the aerosol type information, developing the

732   aerosol type classification algorithm is necessary to make synergy with AEH retrieval.

733   AEH provides representative layer height information as only one variable because of

734   its sole reliance on O_2-O_2 SCD for direct estimation of aerosol height information. This

735   method is limited to the consideration of aerosol vertical structures (i.e., Gaussian or

736   exponential vertical distribution structures). Rather than using the GEMS sensor alone,

737   using another absorption band for oxygen-based materials would provide additional

738   scattering information about aerosols.

739

Data Availability

The TROPOMI ALH product is available from http://doi.org/10.5270/S5P-7g4iapn, and the CALIOP aerosol extinction profile product is available from https://doi.org/10.5067/CALIOP/CALIPSO/CAL_LID_L2_05kmAPro-Prov-V3-41. The GEMS AEH and AERAOD products are available from the Environmental Satellite Center in National Institute of Environmental Research (NIER) of the Republic of Korea.

752 **References**

753 Accarreta, J. R., de Haan, J. F., and Stammes, P.: Cloud pressure retrieval using the O2-
754   O2 absorption band at 477 nm, J. Geophys. Res., 109, D05204,
755   doi:10.1029/2003JD003915, 2004

756 Ahn, C., Torres, O., and Jethva, H.: Assessment of OMI near-UV aerosol optical depth
757   over land, J. Geophys. Res., 119, 2457-2473, 2014.

758 Bogumil, K., Orphal, J., Burrows, J. P., and Flaud, J. M.: Vibrational progressions in the
759   visible and near-ultraviolet absorption spectrum of ozone, Chem. Phys. Lett., 349,
760   241-248, 2001.

761 Buchard, V., de Silva, A. M., Colarco, P. R., Darmenov, A., Randles, C. A., Govindaraju,
762   R., Torres, O., Campbell, J., and Spurr, R.: Using the OMI aerosol index and
763   absorption aerosol optical depth to evaluate the NASA MERRA Aerosol reanalysis,
764   Atmos. Chem. Phys., 15, 5743-5760, 2015.

765 Chen, X., Wang, J., Xu, X., Zhou, M., Zhang, H., Garcia, L. C., Colarco, P. R., Janz, S.
766   J., Yorks, J., McGill, M., Reid, J. S., de Graaf, M., and Kondragunta, S.: First
767   retrieval of absorbing aerosol height over dark target using TROPOMI oxygen B
768   band: Algorithm development and application for surface particulate matter
769   estimates, Remote Sens. Env., 265, 112674, 2021.

770 Chimot, J., Veefkind, J. P., Vlemmix, T., de Haan, J. F., Amiridis, V., Proestakis, E.,
771   Marinou, E., and Levelt, P. F.: An exploratory study on the aerosol height retrieval
772   from OMI measurements of the 477 nm O2-O2 spectral band using a neural
773   network approach, Atmos. Meas. Tech., 10, 783-809, 2017.

774 Choi, H., Liu, X., Abad, G. G., Seo, J., Lee, K. -M., and Kim, J.: A fast retrieval of
775   cloud parameters using a Triplet of wavelengths of oxygen dimer band around 477
776   nm, Remote Sens., 13, 152, doi: 10.3390/rs13010152, 2021.

777 Choi, W., Lee, H., Kim, J., Ryu, J. -Y., Park, S. S., Park, J., and Kang, H.: Effects of
778   spatiotemporal O4 column densities and temperature-dependent O4 absorption
779   cross-section on an aerosol effective height retrieval algorithm using the O4 air
780   mass factor from the ozone monitoring instrument, Remote Sens. Env., 229, 223-
781   233, 2019.

782   Choi, W., Lee, H., and Kim, J.: First TROPOMI retrieval of aerosol effective height
783   using O4 absorption band at 477 nm and aerosol classification, IEEE Trans.
784   Geosci., Remote Sens., 59, 9873-9886, 2021.

785   de Graaf, M., Stammes, P., Torres, O., and Koelemeijer, R. B. A.: Absorbing aerosol
786   index: Sensitivity analysis, application to GOME and comparison with TOMS, J.
787   Geophys. Res., 110, D01201, doi:10.1029/2004JD005178, 2005.

788   de Graaf, M., de Haan, J. F., and Sanders, A. F. J.: TROPOMI ATBD of the Aerosol
789   Layer Height, issue 2.4.0, 2022-04-08,
790   https://sentinel.esa.int/documents/247904/2476257/Sentinel-5P-TROPOMI-
791   ATBD-Aerosol-Height, 75pp, Royal Netherlands Meteorological Institute,
792   Netherland, last access: 15 June, 2024.

793   Ding, S., Wang, J., and Xu, X.: Polarimetric remote sensing in oxygen A and B bands:
794   Sensitivity study and information content analysis for vertical profile of aerosols,
795   Atmos. Meas. Tech, 9, 2077-2092, 2016.

796   Dubuisson, P., Frouin, R., Dessaily, D., Duforet, L., Leon, J. –F., Voss, K., and Antoine,
797   D.: Estimating the altitude of aerosol plumes over the ocean from reflectance ratio
798   measurements in the O2 A-band, Remote Sens. Environ., 113, 1899-1911,
799   doi:10.1016/j.rse.2009.04.018, 2009.

800   European Space Agency, *TROPOMI Level 2 Aerosol Layer Height products. Version*
801   *02.* https://doi.org/10.5270/S5P-7g4iapn, 2021.

802   Gao, Y., Zhao, C., Liu, X., Zhang, M., and Leung, L. R.: WRF-Chem simulations of
803   aerosols and anthropogenic aerosol radiative forcing in East Asia, Atmos. Environ.,
804   92, 250-266, 2014.

805   Geddes, A., and Boesch, H.: Tropospheric aerosol profile information from high-
806   resolution oxygen A-band measurements from space, Atmos. Meas. Tech., 8, 859-
807   874, 2015.

808   Go, S., Kim, J., Park, S. S., Kim, M., Lim, H., Kim, J. -Y., Lee, D. -W., and Im, J.:
809   Synergistic use of hyperspectral UV-visible OMI and broadband meteorological
810   imager MODIS data for a merged aerosol product, Remote Sens., 12, 3987,
811   doi:10.3390/rs12233987, 2020.

812   Griffin, D., Sioris, C., Chen, J., Dickson, N., Kovachik, A., de Graaf, M., Nanda, S.,
813   Veefkind, P., Dammers, E., McLinden, C. A., Makar, P., and Akingunola, A.: The

2018 fire season in North America as seen by TROPOMI: aerosol layer height intercomparisons and evaluation of model-derived plume heights, Atmos. Meas. Tech., 13, 1427-1445, 2020.

Herman, J. R., Bhartia, P. K., Torres, O., Hsu, C., Seftor, C., and Celarier, E.: Global distribution of UV-absorbing aerosols from Nimbus-7/TOMS data, J. Geophys. Res., 102(D14), 16911-16922, 1997.

Hong, H., Lee, H., Kim, J., Jeong, U., Ryu, J., and Lee, D. S.: Investigation of simultaneous effects of aerosol properties and aerosol peak height on the air mass factors for space-borne NO2 retrievals, Remote Sens., 9, 208, doi:10.3390/rs9030208, 2017.

Joiner, J., and Bhartia, P. K.: The determination of cloud pressures from rotational Raman scattering in satellite backscatter ultraviolet measurements, J. Geophys. Res., 100, 23019-23026, 1995.

Joiner, J., and Vasilkov, A. P.: First results from the OMI rotational Raman scattering cloud pressure algorithm, IEEE Trans. Geosci. Remote Sens., 44, 1272-1282, 2006.

Kim, M., Kim, J., Torres, O., Ahn, C., Kim, W., Jeong, U., Go, S., Liu, X., Moon, K. J., and Kim D. -R.: Optimal estimation-based algorithm to retrieve aerosol optical properties for GEMS measurements over Asia, 10, 162, doi:10.3390/rs10020162, 2018.

Kim, J., Jeong, U., Ahn, M. -H., Kim, J. H., Park, R. J., Lee, H., Song, C. H., Choi, Y. -S., Lee, K. -H., Yoo, J. -M., Jeong, M. -J., Park, S. K., Lee, K. -M., Song, C. -K., Kim, S. -W., Kim, Y. J., Kim, S. -W., Kim, M., Go, S., Liu, X., Chance, K., Chan Miller, C., Al-Saadi, J., Veihelmann, B., Bhartia, P. K., Torres, O., González Abad, G., Haffner, D. P., Ko, D. H., Lee, S. H., Woo, J. -H., Chong, H., Park, S. S., Nicks, D., Choi, W. J., Moon, K. -J., Cho, A., Yoon, J., Kim, S. -K., Hong, H., Lee, K., Lee, H., Lee, S., Choi, M., Veefkind, P., Levelt, P. F., Edwards, D. P., Kang, M., Eo, M., Bak, J., Baek, K., Kwon, H. -A., Yang, J., Park, J., Han, K. M., Kim, B. -R., Shin, H. -W., Choi, H., Lee, E., Chong, J., Cha, Y., Koo, J. -H., Irie, H., Hayashida, S., Kasai, Y., Kanaya, Y., Liu, C., Lin, J., Crawford, J. H., Carmichael, G. R., Newchurch, M. J., Lefer, B. L., Herman, J. R., Swap, R. J., Lau, A. K. H., Kurosu, T. P., Jaross, G., Ahlers, B., Dobber, M., McElroy, C. T., and Choi, Y.: New era of

48

845   air quality from Space: Geostationary Environment Monitoring Spectrometer

846   (GEMS), Bul. Ame. Meteorol. Soc., 101(1), E1−E22, 2020.

847   Koffi, B., Schulz, M., Bréon, F.-M., Griesfeller, J., Winker, D., Balkanski, Y., Bauer, S.,

848   Berntsen, T., Chin, M., Collins, W. D., Dentener, F., Diehl, T., Easter, R., Ghan, S.,

849   Ginoux, P., Gong, S., Horowitz, L. W., Iversen, T., Kirkevåg, A., Koch, D., Krol,

850   M., Myhre, G., Stier, P., and Takemura, T.: Application of the CALIOP layer

851   product to evaluate the vertical distribution of aerosols estimated by global models:

852   AeroCom phase I results, J. Geophys. Res.-Atmos., 117,

853   D10201, https://doi.org/10.1029/2011jd016858, 2012.

854   Kokhanovsky, A. A., and Rozanov, V. V.: The determination of dust cloud altitudes from

855   a satellite using hyperspectral measurements in the gaseous absorption band, Int. J.

856   Rem. Sens., 31, Nos. 9-10, 2729-2744, 2010.

857   Kooreman, M. L., Stammes, P., Trees, V., Sneep, M., Tilstra, L. G., de Graaf, M.,

858   Zweers, D. C. S., Wang, P., Tuinder, O. N. E., and Veefkind, J. P.: Effects of cloud

859   on the UV absorbing aerosol index from TROPOMI, Atmos. Meas. Tech., 13,

860   6407-6426, 2020.

861   Lee, J., Kim, J., Song, C. H., Kim, S. B., Chun, Y., Sohn, B. J., and Holben, B. N.:

862   Characteristics of aerosol types from AERONET sunphotometer measurements.

863   Atmos. Env., 44, 3110-3117, 2010.

864   Lorente, A., Boersma, K. F., Yu, H., Doerner, S., Hilboll, A., Richter, A., Liu, M.,

865   Lamsal, L. N., Barkley, M., De Smedt, I., Van Roozendael, M., Wang, Y., Wagner,

866   T., Beirle, S., Liu, J. -T., Krotkov, N., Stammes, P., Wang, P., Eskes, H. J., and Krol,

867   M.: Structural uncertainty in air mass factor calculation for NO2 and HCHO

868   satellite retrieval, Atmos. Meas. Tech., 10, 759-782, 2017.

869   Michailidis, K., Koukouli, M. -E., Balis, D., Veefkind, J. P., de Graaf, M., Mona, L.,

870   Papagianopoulos, N., Pappalardo, G., Tsikoudi, I., Amiridis, V., Marinou, E.,

871   Gialitaki, A., Mamouri, R. -E., Nisantzi, A., Bortoli, D., Joao Costa, M., Salgueiro,

872   V., Papayannis, A., Mylonaki, M., Alados-Arboledas, L., Romano, S., Perrone, M.

873   R., and Baars, H.: Validation of the TROPOMI/S5P aerosol layer height using

874   EARLINET lidars, Atmos. Chem. Phys., 23, 1919-1940, 2023.

875 Nanda, S., de Graaf, M., Sneep, M., de Haan, J. F., Stammes, P., Sanders, A. F. J.,
876   Tuinder, O., Veefkind, J. P., and Levelt, P. F.: Error sources in the retrieval of
877   aerosol information over bright surfaces from satellite measurements in the oxygen
878   A band, Atmos. Meas. Tech., 11, 161–175, https://doi.org/10.5194/amt-11-161-
879   2018, 2018.

880 Nanda, S., de Graaf, M., Veefkind, J. P., Sneep, M., ter Linden, M., Sun, J., and Level, P.
881   F.: A first comparison of TROPOMI aerosol layer height (ALH) to CALIOP data,
882   Atmos. Meas. Tech., 13, 3043-3059, 2020.

883 National Institute of Environmental Research, Geostationary Environment Monitoring
884   Spectrometer (GEMS) Algorithm Theoretical Basis Document: Aerosol Retrieval
885   Algorithm, 42pp, Ministry of Environment, Korea, 2020a.

886 National Institute of Environmental Research, Geostationary Environment Monitoring
887   Spectrometer (GEMS) Algorithm Theoretical Basis Document: Surface
888   Reflectance Algorithm, 35pp, Ministry of Environment, Korea, 2020b.

889 Omar, A., Winker, D. M., Vaughan, M. A., Ju, Y., Trepte, C. R., Ferrare, R. A., Lee, K.-
890   P., Hostetler, C. A., Kittaka, C., Rogers, R. R., Kuehn, R. E., and Liu, Z.: The
891   CALIPSO automated aerosol classification and Lidar ratio selection algorithm, J.
892   Atmos. Ocean. Tech., 26, 10, 1994-2014, 2009.

893 Park, S. S., Kim, J., Lee, H., Torres, O., Lee, K. –M., and Lee, S. D.: Utilization of O4
894   slant column density to derive aerosol layer height from a space-borne UV-visible
895   hyperspectral sensor: Sensitivity and case study, Atmos. Chem. Phys., 16, 1987-
896   2006, doi:10.5194/acp-16-1987-2016, 2016.

897 Park, S. S., Takemura, T., and Kim, J.: Effect of temperature-dependent cross sections
898   on O4 slant column density estimation by a space-borne UV-visible hyperspectral
899   sensor, Atmos. Environ., 152, 98-110, 2017.

900 Park, S. S., Kim, S. -W., Song, C. -K., Park, J. -U., and Bae, K. -H.: Spatio-temporal
901   variability of aerosol optical depth, total ozone, and NO2 over East Asia: Strategy
902   for the validation to the GEMS Scientific Products, Remote Sens., 12, 2256, 2020.

903 Peng, J., Hu, M., Guo, S., Du, Z., Zheng, J., Shang, D., Zamora, M. L., Zeng, L., Shao,
904   M., Wu, Y. -S., Zheng, J., Wang, Y., Glen, C. R., Collins, D. R., Molina, M. J., and
905   Zhang R.: Markedly enhanced absorption and direct radiative forcing of black

906   carbon under polluted urban environments, Proc. Natl. Acad. Sci., 113, 4266-4271,
907   2016.

908 Penning de Vries, M. J. M., Beirle, S., and Wagner, T.: UV aerosol indices from
909   SCIAMACHY: Introducing the Scattering Index (SCI), Atmos. Chem. Phys., 9,
910   9555-9567, 2009.

911 Penning de Vries, M. J. M., Beirle, S., Hoermann, C., Kaiser, J. W., Stammes, P., Tilstra,
912   L. G., Tuinder, O. N. E., and Wagner, T.: A global aerosol classification algorithm
913   incorporating multiple satellite data sets of aerosol and trace gas abundances,
914   Atmos. Chem. Phys., 15, 10597-10618, 2015.

915 Prospero, J. M., Ginoux, P., Torres, O., Nicholson, S. E., and Gill T. E.: Environmental
916   characterization of global sources of atmospheric soil dust identified with the
917   Nimbus 7 total ozone mapping spectrometer (TOMS) absorbing aerosol product,
918   Rev. Geophys., 40, 1002, doi:10.1029/2000RG000095, 2002.

919 Qin, W., Fasnacht, Z., Haffner, D., Vasilkov, A., Joiner, J., Krotkov, N., Fisher, B., and
920   Spurr, R.: A geometry-dependent surface Lambertian-equivalent reflectivity
921   product for UV-vis retrievals – Part 1: Evaluation over land surfaces using
922   measurements from OMI at 466 nm, Atmos. Meas. Tech., 12, 3997-4017, 2019.

923 Rana, A., Jia, S., and Sarkar, S.: Black carbon aerosol in India: A comprehensive review
924   of current status and future prospects, Atmos. Res., 218, 207-230, 2019.

925 Sanders, A. F. J., de Haan, J. F., Sneep, M., Apituley, A., Stammes, P., Vieitez, M. O.,
926   Tilstra, L. G., Tuinder, O. N. E., Koning, C. E., and Veefkind, J. P.: Evaluation of
927   the operational Aerosol Layer Height retrieval algorithm for Sentinel-5 Precursor:
928   application to O2 A band observations from GOME-2A, Atmos. Meas. Tech., 8,
929   4947-4977, 2015.

930 Sanders, A. F. J. and de Haan, J. F.: TROPOMI ATBD of the Aerosol Layer Height
931   product, 2016.

932 Sanghavi, S., Martonchik, J. V., Landgraf, J., and Platt, U.: Retrieval of optical depth
933   and vertical distribution of particulate scatterers in the atmosphere using O2 A- and
934   B-band SCIAMACHY observations over Kanpur: A case study, Atmos. Meas.
935   Tech., 5, 1099-1119, 2012.

936 Spurr, R. "User's Guide VLIDORT Version 2.6, RT Solutions.", Cambridge, MA,
937   USA, 2013.

938 Spurr, R., and Christri, M.: On the generation of atmospheric property Jacobians from
939   the (V)LIDORT linearized radiative transfer models, J. Quant. Spectrosc. Radiat.
940   Transf., 142, 109-115, 2014.

941 Thalman, R., and Volkamer, R.: Temperature dependent absorption cross-sections of
942   O2-O2 collision pairs between 340 and 630 nm and at atmospherically relevant
943   pressure. Phys. Chem. Chem. Phys. 15, 15371e15381, 2013.

944 Torres, O., Bhartia, P. K., Herman, J. R., Ahmad, Z., and Gleason, J.: Derivation of
945   aerosol properties from satellite measurements of backscattered ultraviolet
946   radiation: Theoretical basis, J. Geophys. Res., 103(14), 17099-17110, 1998.

947 Torres, O., Decae, R., Veefkind, P., and de Leeuw, G.: OMI Aerosol Retrieval Algorithm,
948   OMI Algorithm Theoretical Basis Document, Vol. III, Clouds, Aerosols and
949   Surface UV Irradiance, NASA-KNMI ATBD-OMI-03, pp. 47-71, 2002.

950 Torres, O., Jethva, H., Ahn, C., Jaross, G., and Loyola, D. G.: TROPOMI aerosol
951   products: evaluation and observations of synoptic-scale carbonaceous aerosol
952   plumes during 2018-2020, Atmos. Meas. Tech., 13, 6789-6806, 2020.

953 Vandaele, A. C., Hermans, C., Simon, P. C., Carleer, M., Colin, R., Fally, S., Merienne,
954   M. F., Jenouvrier, A., and Coquart, B.: Measurements of the NO2 absorption cross-
955   section from 42000 cm-1 to 10000 cm-1 (238-1000 nm) at 220 K and 294 K, J.
956   Quant. Spectrosc. Radiat. Transfer, 59, 3-5, 171-184, 1998.

957 Vasilkov, A., Joiner, J., Spurr, R., Bhartia, P. K., Levelt, P., and Stephens, G.: Evaluation
958   of the OMI cloud pressures derived from rotational Raman scattering by
959   comparisons with other satellite data and radiative transfer simulations, J. Geophys.
960   Res., 113, D15S19, doi:10.1029/2007JD008689, 2008.

961 Vasilkov, A., Yang, E. -S., Marchenko, S., Qin, W., Lamsal, L., Joiner, J., Krotkov, N.,
962   Haffner, D., Bhartia, P. K., and Spurr, R.: A cloud algorithm based on the O2-O2
963   477 nm absorption band featuring an advanced spectral fitting method and the use
964   of surface geometry-dependent Lambertian-equivalent reflectivity, Atmos. Meas.
965   Tech., 11, 4093-4107, 2018.

966 Veefkind, J. P., Aben, I., McMullan, K., Foerster, H., de Vries, J., Otter, G., Claas, J.,
967   Eskes, H. J., de Haan, J. F., Kleipool, Q., van Weele, M., Hasekamp, O.,
968   Hoogeveen, R., Landgraf, J., Snel, R., Tol, P., Ingmann, P., Voors, R., Kruizinga, B.,
969   Vink, R., Visser, H., and Levelt, P. F.: TROPOMI on the ESA Sentinel-5 Precursor:

A GMES mission for global observations of the atmospheric composition for climate, air quality and ozone layer applications, Remote Sens. Env., 120, 70-83, 2012.

Veihelmann, B., Levelt, P. F., Stammes, P., and Veefkind, J. P.: Simulation study of the aerosol information content in OMI spectral reflectance measurements, Atmos. Chem. Phys., 7, 3115-3127, 2007.

Wang, R., Tao, S., Wang, W., Liu, J., Shen, H., Shen, G., Wang, B., Liu, X., Li, W., Huang, Y., Zhang, Y., Lu, Y., Chen, H., Chen, Y., Wang, C., Zhu, D., Wang, X., Li, B., Liu, W., and M, J.: Black carbon emissions in China from 1949 to 2050, Environ., Sci. Technol., 46, 7595-7603, 2012.

Winker, D. M., Vaughan, M. A., Omar, A. H., Hu, Y., Powell, K. A., Liu, Z., Hunt, W. H., and Young, S. A.: Overview of the CALIPSO mission and CALIOP data processing algorithms, J. Atmos. Oceanic Technol., 26, 2310-2323, 2009.

Xu, X., Wang, J., Wang, Y., Zeng, J., Torres, O., Reid, J. S., Miller, S. D., Martins, J. V., and Remer, L. A.: Detecting layer height of smoke aerosols over vegetated land and water surfaces via oxygen absorption bands: hourly results from EPIC/DSCOVR in deep space, Atmos. Meas. Tech., 12, 3269-3288, 2019.

Zeng, Z. -C., Chen, S., Natraj, V., Le, T., Xu, F., Merrelli, A., Crisp, D., Sander, S. P., and Yung, Y. L.: Constraining the vertical distribution of coastal dust aerosol using OCO-2 O_2 A-band measurements, Remote Sens. Env., 236, 111494, 2020.